Nanoscale

Accepted Manuscript

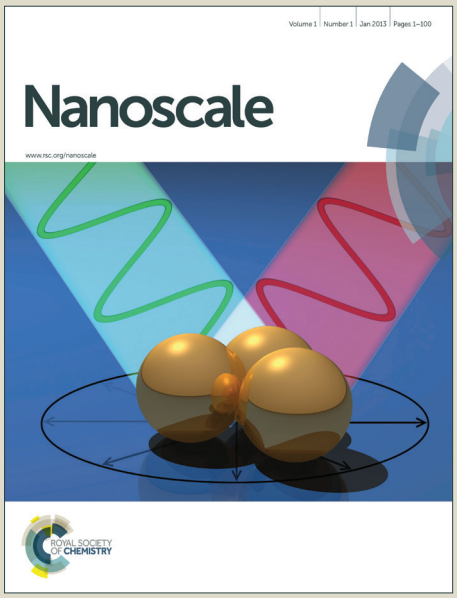

Insights from Investigations of Tin Dioxide and Their Composites: Electron-Beam Irradiation, Fractal Assessment, and Mechanism

Zhiwen Chen,[*a,b] Chan-Hung Shek,[b] C. M. Lawrence Wu[*b]

[a] School of Environmental and Chemical Engineering, Shanghai University, Shanghai 200444, People's Republic of China

[b] Department of Physics and Materials Science, City University of Hong Kong, Tat Chee Avenue, Kowloon Tong, Hong Kong

*Corresponding authors. Tel.: +86 21 66137503. Fax: +86 21 66137787. E-mail: zwchen@shu.edu.cn; apcmlwu@cityu.edu.hk.

[a] School of Environmental and Chemical Engineering, Shanghai University, Shanghai 200444, People's Republic of China

[b] Department of Physics and Materials Science, City University of Hong Kong, Tat Chee Avenue, Kowloon Tong, Hong Kong

Abstract

Tin dioxide (SnO_2) is unique strategic functional materials with widespread technological applications, particularly in the fields such as solar battery, optoelectronic devices, and solid-state gas sensors owing to advances in optical and electronic properties. In this review, we introduce recent progresses of tin dioxide and their composites, including the synthesis strategies, microstructual evolution, related formation mechanism, and performance evaluation of SnO_2 quantum dots (QDs), thin films, and composites prepared by electron-beam irradiation, pulsed laser ablation, and SnO_2 planted graphene strategies, highlighting contributions from our laboratory. First, we present the electron-beam irradiation strategies for growth behavior of SnO_2 nanocrystals. This method is a potentially powerful technique to achieve the nucleation and growth of SnO_2 QDs. In addition, the fractal assessment strategies and gas sensing behavior of SnO_2 thin films with interesting micro/nanostructures induced by pulsed delivery will be discussed experimentally and theoretically. Finally, we emphasize the fabrication process and formation mechanism of SnO_2 QDs planted graphene nanosheets. This review may provide a new insight that the versatile strategies for microstructural evolution and related performance of SnO_2-based functional materials are of fundamental importance in the development of new materials.

Keywords: Tin dioxide; Electron-beam irradiation; Fractal assessment; SnO_2 planted graphene; Microstructure; Mechanism

1. Introduction

1.1. Preamble

Semiconductor oxides are fundamental to the development of smart and functional materials, devices, and systems.[1-4] These oxide materials have two unique structural features: mixed cation valences and an adjustable oxygen deficiency, which are the bases for creating and tuning many novel material properties, from chemical to physical.[5-7] Developing new materials with excellent performances depend not only on the multi-components but also on their micro/nanostructures. Multi-components and micro/nanostructures are the key issues to realize multifunctional materials. The key scientific issues of tin dioxide (SnO_2) functional materials and their applications and developments have been driven scientists to explore continuously in depth their preparation, micro/nanostructure and performances. SnO_2, as a kind of *n*-type wide-band-gap semiconductor (E_g = 3.64 eV at 300 K), has very wide applications in the fields such as solid-state gas sensors,[8] luminescent materials,[9] solar battery,[10] antistatic coating,[11] and optoelectronic devices.[12] Since the properties of materials strongly depend on its micro/nanostructures, which all result from the fabrication processes, the influence of micro/nanostructural evolution on material properties is especially remarkable for materials science and engineering. Tin oxide micro/nanostructures provide a versatile, multifaceted platform for a broad range of advanced applications.[13-15] Recent studies have validated their use in many fields of science and technology that integrate the areas of chemistry, physics, materials science and nanotechnology.[16-20] For example, they can function as semiconductors for a number of applications in microelectronic devices, optoelectronic components, and solar-thermal converter, they can serve as gas-sensors for the detection and forecasting of a variety of combustible gases, environmental pollution gases, industrial emissions and hazardous gases, they can used as electrodes for melting optical glass and electrolytic aluminum industry, they can act as catalysts for the active phase of many heterogeneous catalysis in hydrocarbon oxidation, they can also serve as varistor for the arrester used in power systems, and so on.

However, challenges remain to further improve the material fabrication processes for various advanced applications. This optimization requires a clear understanding of the relationship between micro/nanostructures and preparation conditions.

In this review, we will describe our efforts toward understanding the synthesis strategies, microstructual evolution, related formation mechanism, and performance evaluation of SnO_2 various morphologies including SnO_2 quantum dots (QDs), thin films, and composites prepared by electron-beam irradiation (EBI), pulsed laser ablation, and SnO_2 planted graphene strategies, highlighting contributions from our laboratory. Fig. 1 shows schematic illustrating in this article including SnO_2 electron-beam irradiation strategies, fractal assessment and SnO_2 planted graphene strategies. In sections 2, we present the EBI strategies for growth behavior of SnO_2 nanocrystals. This method is a potentially powerful technique to achieve the nucleation and growth of SnO_2 QDs. In sections 3, the fractal assessment strategies and gas sensing behavior of SnO_2 thin films with interesting micro/nanostructures induced by pulsed delivery will be discussed experimentally and theoretically. In sections 4, we emphasize the fabrication process and formation mechanism of SnO_2 QDs planted graphene nanosheets. This review may provide a new insight that the versatile strategies for microstructural evolution and related performance of SnO_2-based functional materials are of fundamental importance in the development of new materials.

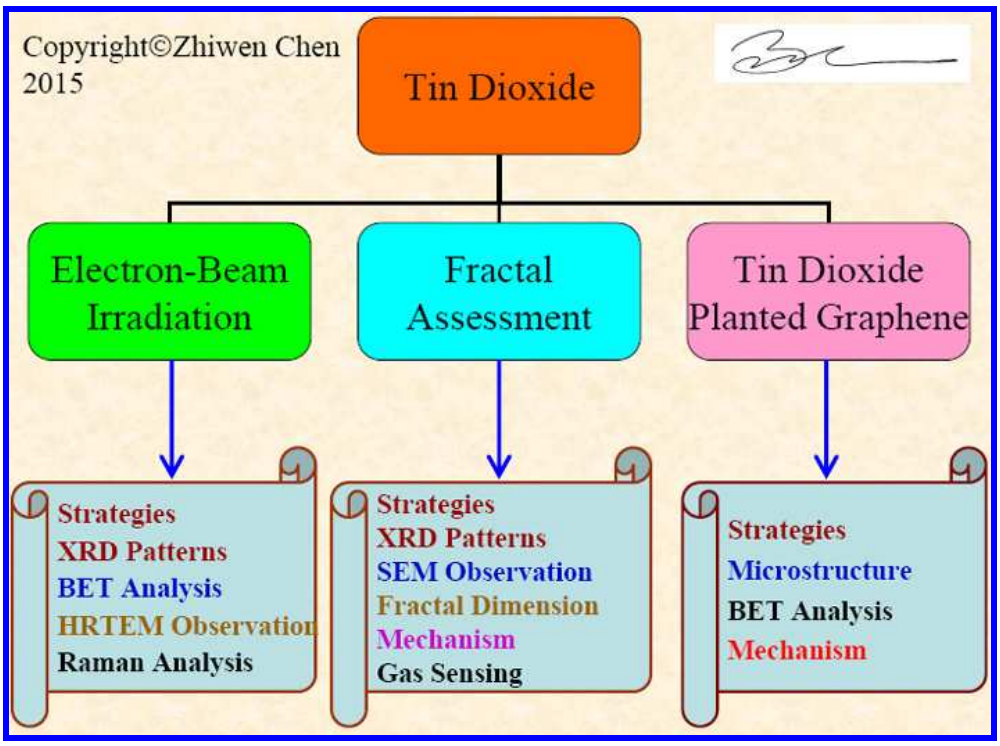

Fig. 1. Schematic illustrating in this article including SnO_2 electron-beam irradiation strategies, fractal assessment and SnO_2 planted graphene strategies.

1.2. Outline

This review presents some advanced developments in the synthesis strategies and perspectives of microstructual evolution, related formation mechanism, and performance evaluation for SnO_2 various morphologies including SnO_2 QDs, thin films, and composites. This is an interdisciplinary work that integrates the areas of physics, chemistry and materials science. A brief outline of the contents and organization of each section is presented here to serve as a guide for reading this article.

The major aim in section 2 is to explore the EBI strategies for growth behavior of SnO_2 nanocrystals. In this section, we will describe in detail that the SnO_2 nanocrystals prepared by sol-gel method are radiated by electron accelerator. The microstructural evolution of SnO_2 nanocrystals was evaluated by

XRD, HRTEM, Raman, thermo gravimetric-differential scanning calorimeter, and automated surface area analyzer. The characterization analysis indicated that the crystallinity of the irradiated SnO_2 powders was better than unirradiated one. The clear lattice fringes of SnO_2 QDs were investigated in detail by HRTEM. It was found that the sizes of SnO_2 QDs were localized in the range of 2-4 nm. The Brunauer-Emmett-Teller (BET) surface area analysis indicated that the specific surface area of irradiated sample was much higher, which was almost doubled at 1400 kGy under the 8 mA/s of irradiation rate and 50 seconds of irradiation time.

The purpose of the section 3 is to characterize the dependence of gas sensing behavior on fractal dimension in SnO_2 thin films induced by pulsed delivery. SnO_2 thin films with interesting fractal features were prepared by pulsed laser deposition techniques under different substrate temperatures. The fractal assessments indicated that the fractal theory can be applied to the evaluation of this material. The measurements of carbon monoxide gas sensitivity confirmed that the gas sensing behavior was sensitively dependent on fractal dimensions, fractal densities, and average sizes of the fractal clusters. Random Tunneling Junction Network (RTJN) mechanism was suggested to provide a rational explanation for this gas sensing behavior. The formation process of SnO_2 nanocrystals and fractal clusters were reasonably discussed by the use of a model.

In section 4, we present the assembling SnO_2 QDs to graphene nanosheets (GNSs) by a facile ultrasonic method. The experimental investigations indicated that the graphene was exfoliated and decorated with SnO_2 QDs, which was dispersed uniformly on both sides of graphene. The size distribution of SnO_2 QDs was estimated to be a ranging from 4 to 6 nm and their average size was calculated to be about 4.8 ± 0.2 nm. This facile ultrasonic route demonstrated that the loading of SnO_2 QDs was an effective way to prevent the GNSs from being restacked during the reduction. During the calcination process, the GNSs distributed between SnO_2 nanoparticles have also prevented the agglomeration of SnO_2 nanoparticles, which were beneficial to the formation of SnO_2 QDs.

2. Electron-Beam Irradiation Strategies for Tin Dioxide

2.1. Overview on Tin Dioxide Quantum Dots

SnO_2, as a kind of *n*-type semiconductor, has very wide applications in the fields such as solid-state gas sensors,[21] luminescent material,[22] solar battery,[23] antistatic coating,[24] and optoelectronic devices[25] owing to their unique electronic, optical, and magnetic properties. During the past decade, a lot of methods such as sol-gel,[26] chemical vapor deposition,[27] spray pyrolysis,[28] hydrothermal method,[29] and microwave technique,[30] have been employed to prepare SnO_2 nanostructures. It is common that the grain sizes and morphologies of nanomaterials greatly affect their properties as well as their applications. For example, when the size of the particle decreased, the surface-volume ratio and the band gap will increase correspondingly, such effect will finally lead to the enhancement of the gas sensors sensitivity. Therefore, the quantum size effects particularly in the semiconductor quantum dots have enhanced great interest in both basic and applied research.[31] Several studies on quantum dot (QD) systems were carried out in the last decade mainly on GaAs, InP, and Cd chalcogenides due to their discrete electronic states, unusual structural transformations and novel physical and chemical properties.[32] It is well-known that the size of QDs is usually among from 1 nm to 10 nm particularly if the critical dimensions approach the exciton Bohr radius of nanomaterials which carriers are confined in all three dimensions to a nanometer-sized region. Thus, the QDs exhibit distinctive properties as well as have a wide range applications in optoelectronics, optical sensors and lasers.[33,34] For this reason, the properties of oxide semiconductors with wide-band-gap QDs have been growing attracted much attention such as nanocrystalline SnO_2. In a variety of SnO_2 QD synthesis processes, Castillo and co-workers reported on the preparation of SnO_2 QDs with the sizes in 2-5 nm by the sol-gel method.[35] Zhu and co-workers obtained the SnO_2 QDs with the sizes in 2.3-3.1 nm by hydrothermal process.[34]

The irradiation technique achieved by electron accelerator is of widespread technological applications in the fields of degraded organic compounds, medical treatment, industrial and agricultural applications.[36] Up to now, there are few reports related tin oxide modified by accelerator radiation. It is well-known that the EBI method has a number of high advantageous properties. For instance, (i) this method is simple, rapid and convenient,[37] (ii) it is carried out at room temperature without any kind of catalysts, and (iii) the method is useful for the mass-production of nanomaterials. After an extensive search in the published literature, it was found that the previous nanocrystals are assembled either aqueous synthesis, hydrothermal, and pyrolysis or epitaxial approaches through the gas phase. Compared with the previous heat-treatment technique which is a commonly used crystallization method, the production of SnO_2 QDs by the EBI method has also attracted much attention due to above many advantages. In order to investigate the characteristics of these QDs, the microstructure evolution of SnO_2 nanocrystals should be reasonably understood. An integrated device for different QDs is highly desirable for versatile advanced applications. Despite the high sensitivity of SnO_2 to many gases, it is often susceptible to electrical drift which requires long stabilization periods, as well as permanent poisoning after extended periods of operation. EBI may be a potentially powerful technique to modify QDs, and we are applying this technique to SnO_2 nanocrystals for the first time in this study.[38]

2.2. Electron-Beam Irradiation Strategies

A typical procedure to synthesize SnO_2 nanoparticles via sol-gel method was performed as follows. Under intensive stirring, aqueous ammonia (2 mol/L) was drop wisely added into $SnCl_4$ solution (0.2 mol/L) until pH reached 7. The reaction temperature was kept at 60 ^{o}C. The primal sample was centrifuged and rinsed with alcohol and deionized water several times till the Cl^- could not be detected

by $AgNO_3$ solution, and then dried at 80 °C in the vacuum drying chamber for 10 h. The products were collected after being ground into fine powder. Basic process is shown below:

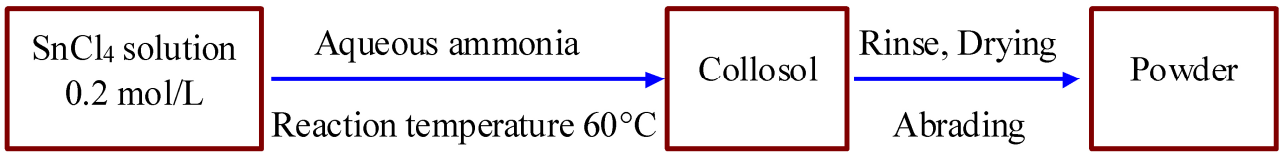

The as-prepared SnO_2 nanoparticles was dispersed as much as possible to thickness with 2-3 mm, which was placed under the Titanium window of GJ-2-II Dynamitron electron accelerator with an accelerating voltage of 2 MeV and a current of 8 mA by different radiation dose.

2.3. XRD and BET Analysis

It is known that the SnO_2 has a tetragonal rutile crystalline structure (known in its mineral form as cassiterite) with point group D_{4h}^{14} and space group $P4_2/mnm$. The lattice parameters are $a = b =$ 4.7382(4) Å, and c = 3.1871(1) Å.[39] Fig. 2 shows the typical XRD patterns of SnO_2 powders (a) as-prepared (unirradiated) sample and (b) irradiated sample which was irradiated at 1400 kGy under the irradiation rate 8 mA/s and irradiation time 50 seconds. Through a series of experiments, it can be found that the SnO_2 powders have obviously changed under 1400 kGy dose comparing with the as-prepared (unirradiated) powders. All diffraction peaks can be attributed to the tetragonal SnO_2 structure with cell parameters $a = b$ = 4.738 Å and c = 3.187 Å, which is consistent with the standard card (JCPDS file No.41-1445). The XRD patterns as shown in Fig. 2b reveal the stronger peak intensity and smaller peak width, which indicated that the irradiated SnO_2 nanoparticles have better crystallizing.[40] The presence of broad and weak peaks as shown in Fig. 2a also indicates that the unirradiated SnO_2 nanoparticles smaller than irradiated one because of the width of XRD peaks is related to particle size through Scherrer's equation: $D = K\lambda / \beta \cos\theta$, where D is the diameter of the nanoparticles, K = 0.9, λ

(Cu K_α) = 1.5406 Å, and β is the full width at half maximum of the diffraction peak.[41] Comparing with Fig. 2a and b, it confirmed that the growth of SnO_2 nanocrystals is influenced significantly by the EBI techniques. All peaks as shown in Fig. 2b became sharp and stronger, and appeared some new peaks proved that the EBI is a potentially powerful technique to improve the growth of SnO_2 nanocrystals.

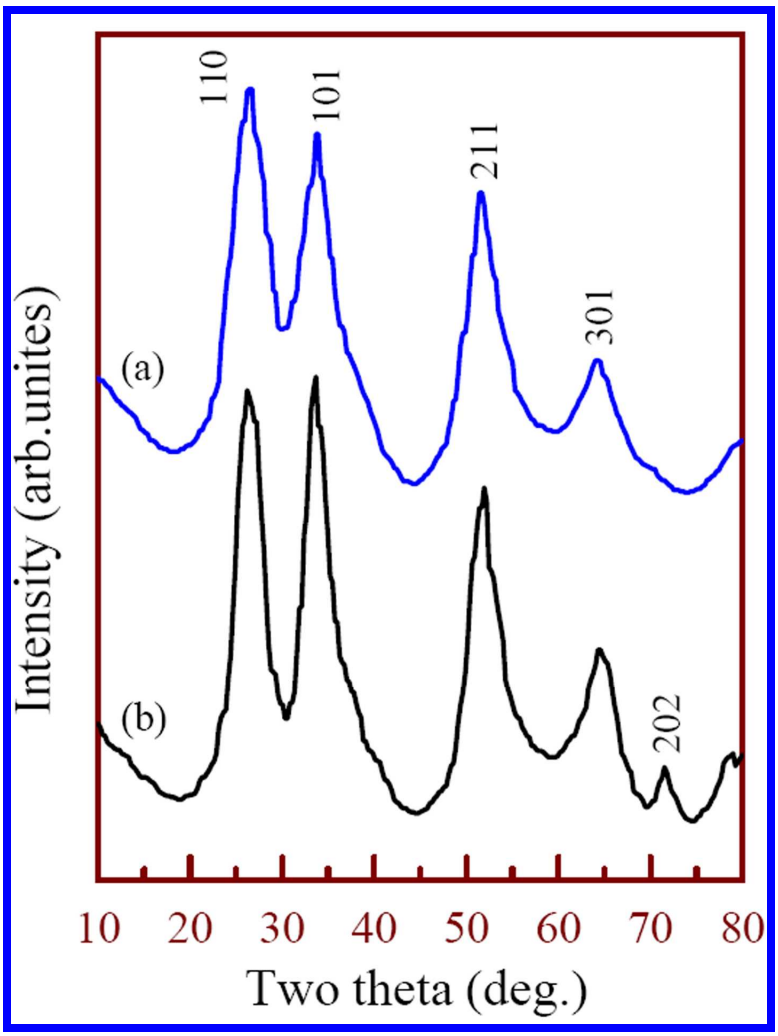

Fig. 2. The typical XRD patterns of SnO_2 powders (a) as-prepared (unirradiated) sample, (b) irradiated sample which was irradiated at 1400 kGy under the irradiation rate 8 mA/s and irradiation time 50 seconds.[38]

Thermo-analysis of the as-prepared (unirradiated) and irradiated SnO_2 powders has been given in Fig. 3a and b, respectively. As shown in Fig. 3b, the thermo gravimetric (TG) analysis of irradiated SnO_2 powders showed that the amount of weight loss (the mass loss ~17%) is smaller than unirradiated one (the mass loss ~22.3%), which indicated that the irradiated SnO_2 powders have been further crystallized during EBI processes. For both samples studied in TG-DTG experiments, it was found that the shapes of the TG-DTG curves are similar but exist still obviously difference. For instance, the observed weight loss of two samples between room temperature to 350 ^{o}C may be attributed to the loss of ammonia, physically absorbed water and chemically bonded water,[30] which corresponds with the endothermic peak at about 200 ^{o}C in DSC curves. Moreover, the DTG peaks of the irradiated SnO_2 have a minor right shift comparing with the as-prepared SnO_2, which indicated that the as-prepared SnO_2 is poor crystalline.[42] According to the formula: $(dH/dT)/(dT/dt) = dH/dT = C_p$, while dH/dt for the DSC spectrum of the vertical axis, dT/dt is rise/cooling rate, C_p is specific heat capacity at constant pressure, showing the specific heat of the grains in the relative size at this time. Thus, it determined that the heat absorption capacity during crystallization of irradiated sample is much larger than the unirradiated one. Comparing with previous researches such as Zhu and co-workers reported an endothermic peak at a temperature about 90 ^{o}C of the DSC curve for SnO_2 nanoparticles[43] and Zeng and co-workers showed two endothermic peaks at 532 and 556 K.[44] There were significant differences as the presented irradiated SnO_2 that revealed two obvious exothermic peaks at temperatures of 78 ^{o}C and 910 ^{o}C. However, the exothermic peak of the as-prepared SnO_2 shifted to 71 ^{o}C, moreover it was not obviously. In addition, one of endothermic peaks nearly in 180 ^{o}C corresponds to the removal of water while the endothermic peak of DSC curves for the as-prepared SnO_2 is flatter, which indicated that less activity center is formed.[45]

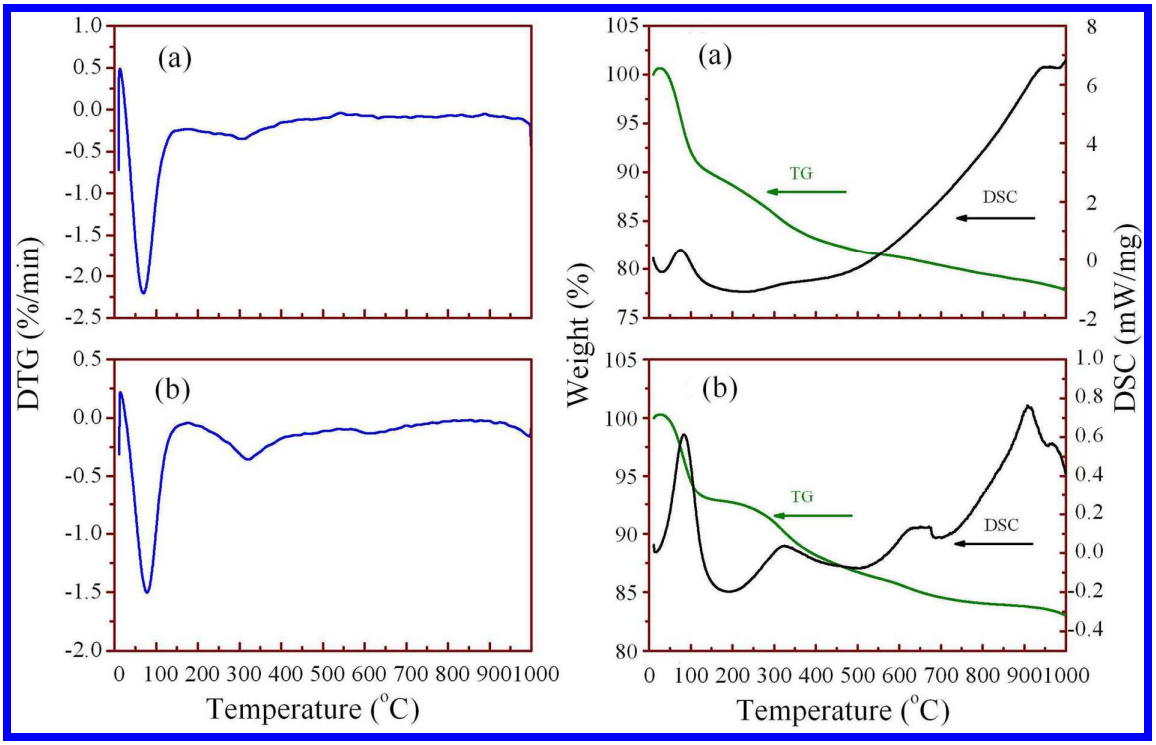

Fig. 3. The TG-DTG-DSC curves of SnO_2 powders (a) as-prepared (unirradiated) sample, (b) irradiated sample which was irradiated at 1400 kGy under the irradiation rate 8 mA/s and irradiation time 50 seconds.[38]

Fig. 4 shows the specific surface areas of the as-prepared (unirradiated) sample and irradiated samples with different radiation doses under the irradiation rate 8 mA/s. It can be seen that the as-prepared sample has the lower surface area than the irradiated samples. When the irradiated dose increased to 700 kGy under the irradiation rate 8 mA/s and irradiation time 25 seconds, the BET surface area increased from 105.39 m^2/g to 170.47 m^2/g. However, the BET value has slightly decreased to 165.42 m^2/g at 980 kGy radiation dose under the irradiation rate 8 mA/s and irradiation time 35 seconds. From view in the overall trend of BET values, it can be reasonable to speculate that the more SnO_2 crystal nucleus could be formed in irradiated samples, which can also be proved by the HRTEM results as shown in Fig. 5. The more smaller SnO_2 crystal nucleus, which may be called as

SnO_2 QDs, led to the increasing of the BET surface area of irradiated samples. However, when the irradiated dose increased to 980 kGy, the rotation and coalescence processes of the initial SnO_2 crystal nucleus (e.g. at 700 kGy) culminating in a low-energy configuration may be directly related to the reduction of surface energy, aimed at minimizing the area of high-energy interfaces.[46,47] The possible formation of a coherent boundary between grains due to the grain rotation, with the consequence of removing the common grain boundary and culminating in a single larger SnO_2 nanocrystal, may lead to the decreasing of the BET value. With the increasing of the irradiated doses, for example, 1260 and 1400 kGy under the irradiation rate 8 mA/s and irradiation times 45 and 50 seconds, respectively, a large number of SnO_2 crystal nucleus could be formed in irradiated samples. Therefore, the BET values increased. The BET analysis indicated that the specific surface area of the irradiated samples tends to increase as the increasing of the irradiated doses. It implied that the EBI method can significantly enhance the BET surface area.

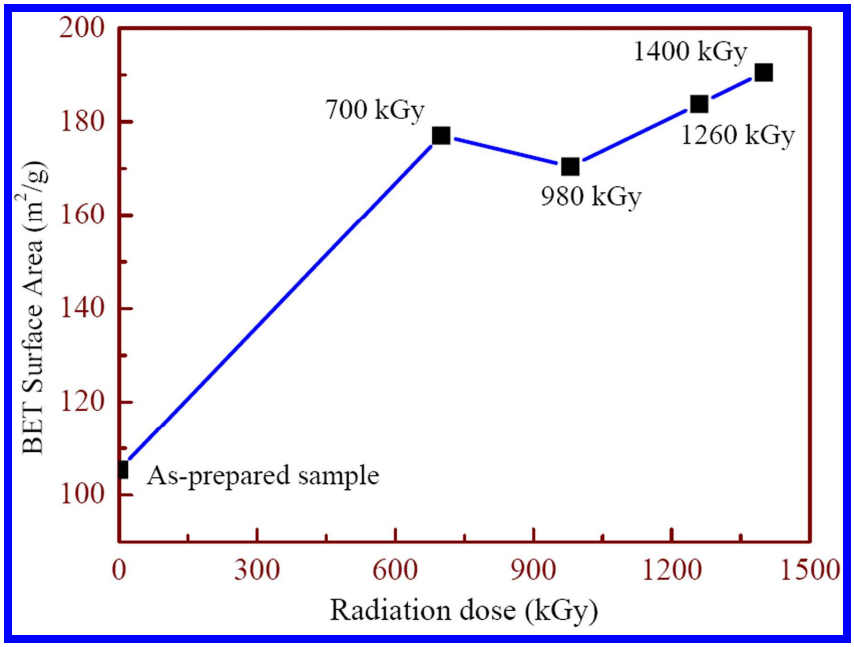

Fig. 4. Specific surface area of as-prepared (unirradiated) sample and irradiated samples at 700, 980, 1260 and 1400 kGy under the irradiation rate 8 mA/s and irradiation times 25, 35, 45, and 50 seconds, respectively.[38]

2.4. HRTEM and Raman Examination

Since detailed and refined experiments on SnO_2 nanocrystals permitted us to assess the physics of quantum-confined excitations, the geometry and nature of the contact areas between SnO_2 particles (unirradiated and irradiated samples) are especially important for the steady state optical gain in small semiconductor wide-band-gap QDs. Fig. 5 displays the HRTEM images of SnO_2 powders (a) as-prepared (unirradiated) sample and (b) irradiated sample which was irradiated at 1400 kGy under the irradiation rate 8 mA/s and irradiation time 50 seconds. It was found that the SnO_2 QDs can be formed in the as-prepared (unirradiated) and irradiated samples (indicated by the blue circles). The clear lattice fringes demonstrated that the SnO_2 QDs are composed of ultrafine nanoparticles with a diameter below 4 nm. Comparison of Fig. 5a and b, the samples modified by EBI revealed clear-cut crystalline features and more clearly crystal planes which could correspond to the lattice parameters of the rutile structure of SnO_2 cassiterite phase. The results indicated that the density and size of the SnO_2 QDs increase after the EBI. HRTEM analysis indicated that the crystal planes of the QDs become more complete. The inset at the lower right-hand corner in Fig. 5b shows two QDs with size of about 4 nm and 3.5 nm. The interplanar spacings are about 0.33 nm and 0.26 nm which respectively correspond to the (110) and (101) planes of tetragonal SnO_2. More importantly, HRTEM observation in the sample modified by EBI is very interesting. Fig. 5b shows the initial stage of the SnO_2 crystal nucleus and QD growth processes. The white arrow in blue circles indicated the formation of necks between QDs. An analysis suggested that the first step in the QD growth process is the formation of necks. After this step, a rotation may occur to decrease the angle of misorientation, changing the QD orientation. When the QDs approach the same orientation, i.e., a coherent grain-grain boundary, the grain boundary must migrate toward the smaller crystal nucleus, resulting in a single larger QD. Therefore, the EBI method is a potentially powerful technique to achieve SnO_2 nucleation and QD growth.

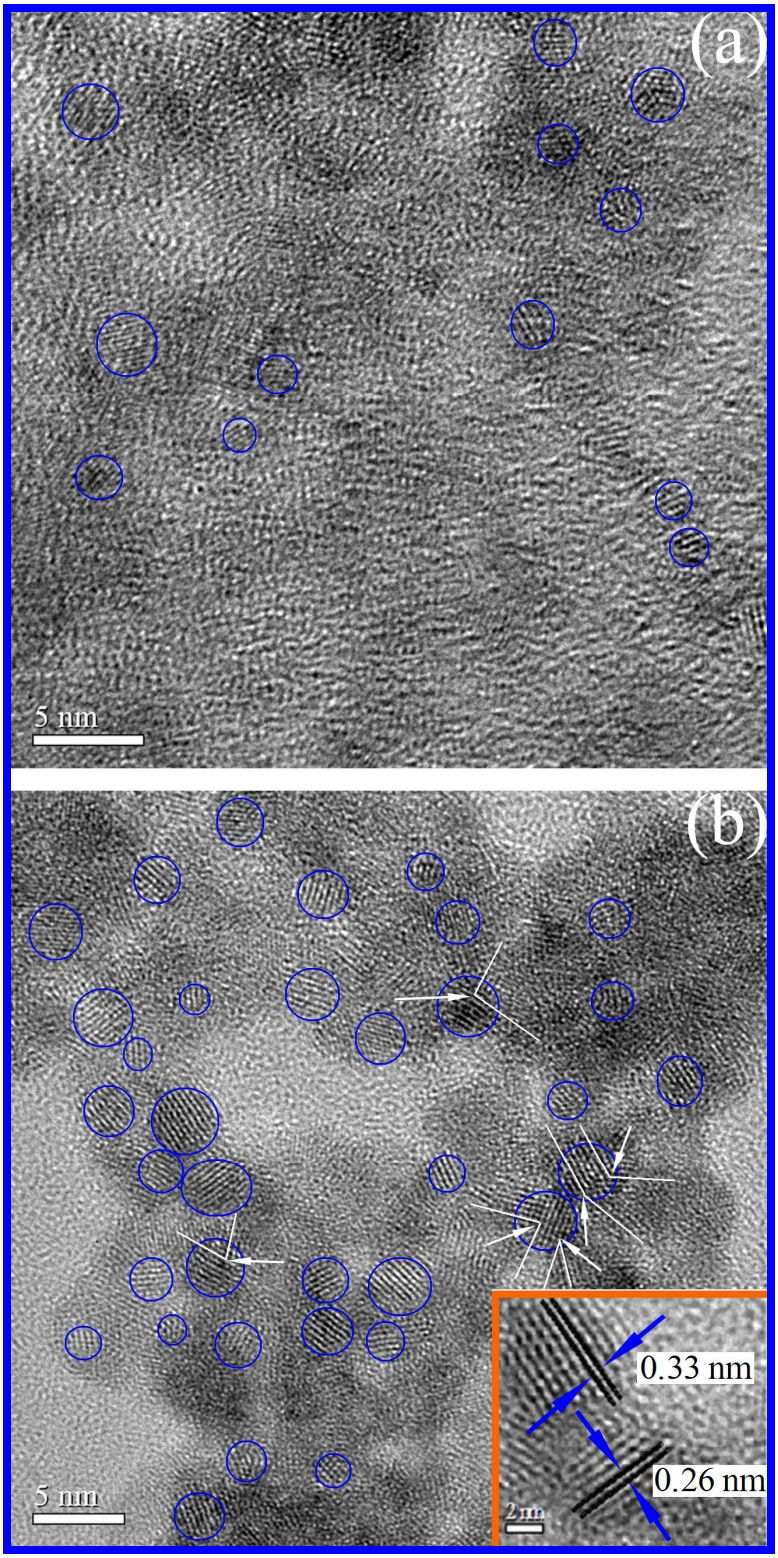

Fig. 5. HRTEM images of SnO_2 powders (a) as-prepared (unirradiated) sample, (b) irradiated sample which was irradiated at 1400 kGy under the irradiation rate 8 mA/s and irradiation time 50 seconds.[38]

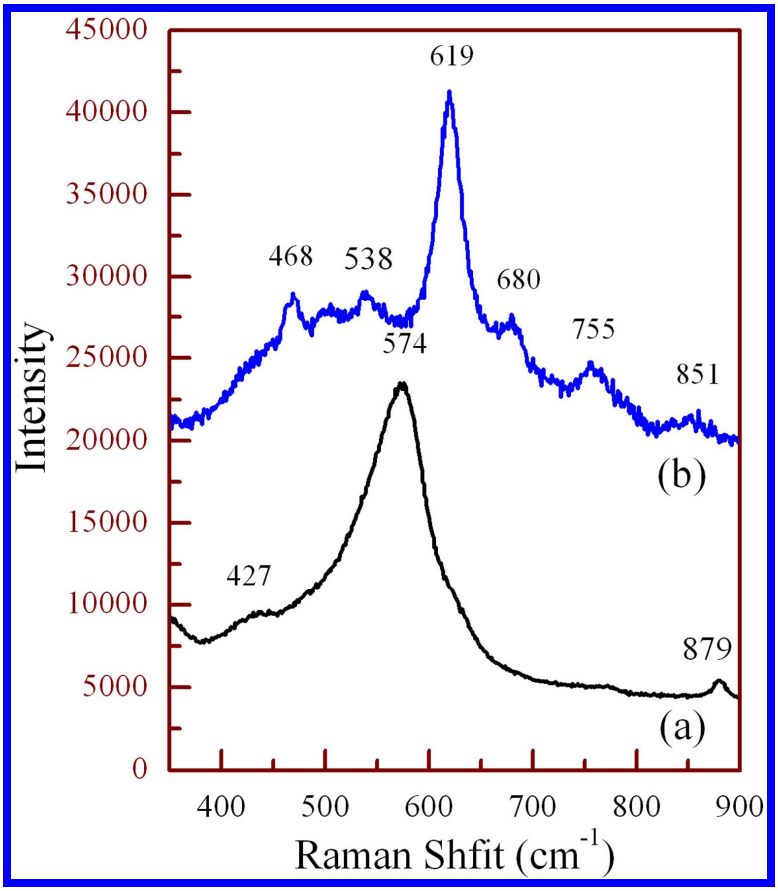

Fig. 6. Room-temperature Raman spectra of (a) as-prepared (unirradiated) sample, (b) irradiated sample which was irradiated at 1400 kGy under the irradiation rate 8 mA/s and irradiation time 50 seconds.[38]

In order to obtain further information on the microstructure evolution of SnO_2 powders modified by the EBI, Raman techniques could effectively reveal local structural features of amorphous and poorly crystallized materials owing to its fine sensitive to crystal surface area.[41] Fig. 6 shows room-temperature Raman spectra of (a) as-prepared (unirradiated) sample and (b) irradiated sample which was irradiated at 1400 kGy under the irradiation rate 8 mA/s and irradiation time 50 seconds. It can be seen that the irradiated sample shown in Fig. 6b presents five Raman peaks at 468, 538, 619, 680, 755 and 851 cm^{-1} in contrast to the as-prepared (unirradiated) sample shown in Fig. 6a just presents three

Raman peaks at 427, 574 and 879 cm^{-1}. In general, the SnO_2 unit cell consists of two metal atoms and four oxygen atoms. Each metal atom is situated amidst six oxygen atoms which approximately form the corners of a regular octahedron. Oxygen atoms are surrounded by three tin atoms which approximate the corners of an equilateral triangle. As a result, there are 18 branches for the vibrational modes in the first Brillouin zone. The normal vibration modes at the Γ point at the center of the Brillouin zone is given by[47]

$$\Gamma = \Gamma_1^+(A_{1g}) + \Gamma_2^+(A_{2g}) + \Gamma_3^+(B_{1g}) + \Gamma_4^+(B_{2g}) + \Gamma_5^+(E_g) + 2\Gamma_1^+(A_{2u}) + 2\Gamma_4^+(B_{1u}) + 4\Gamma_5^+(E_u).$$

According to these modes, A_{1g}, B_{1g}, B_{2g} and E_g are Raman active, A_{2u}, E_u and B_{1u} are active in infrared (IR), one A_{2u} and two E_u modes are acoustic. Raman peaks at 468, 619 and 777 cm^{-1} in Fig. 6b can be indexed to E_g, A_{1g} and B_{2g} vibration modes, respectively.[48] In addition, the other Raman peaks at 538 and 680 cm^{-1} also were observed, which may be close to the IR-actived A_{2u} modes at 512 cm^{-1} for transverse-optical (TO), and at 687 cm^{-1} for longitudinal-optical (LO).[49] In a perfect crystal, only is the center of Brillouin zone (q = 0) phonon can be excited because the correlation length of the particular phonon is infinite. In the nanocrystals, some IR active modes may transform into Raman active with decreasing size and increasing disorder for the nanomaterials. Thus, Raman scattering intensity of lattice vibration is[50]

$$I(\omega) \propto \int_0^1 \exp\left|-\frac{q^2L^2}{4}\right| \frac{dq^3}{[\omega-\omega(q)]^2 + [\Gamma_0/2]^2},$$

and

$$\omega(q) = A + B\cos(\Pi q),$$

where ω is phonon frequency, q is phonon wave vector, $\omega(q)$ is the phonon dispersion curve of the infinite crystal, Γ_0 is the natural line width, and L for the coherence length. Abello and co-workers have reported that some vibration modes forbidden in the theory would be activated when the dimension of the grains is small enough, especially, some IR-active modes may be weakened to show Raman-

active.[51] In our Raman experiments, the as-prepared (unirradiated) sample shown in Fig. 6a has three peaks, which there is a few research on the peak of 574, it may be the peak displacemen of amorphous SnO_2.[52] However, the irradiated sample shown in Fig. 6b has a obvious blue shift compared with Fig. 6a. This may attributed to relaxation of Raman selection rule due to the combined effects in the increasing of QD density and the high concentration of defects in surface site, such as oxygen vacancies and lattice disorder.[51]

3. Fractal Assessment Strategies for Tin Dioxide

3.1. Overview on Tin Dioxide Tin Films

Semiconductor oxides are fundamental to the development of smart and functional materials, devices, and systems.[53-55] These oxides have two unique structural features: mixed cation valences and an adjustable oxygen deficiency, which are the bases for creating and tuning many novel material properties, from chemical to physical.[56-58] Due to the increasing importance of air pollution and the need to monitor concentration levels of gases such as CO, CO_2, NO_x, O_3, SO_2 etc., the development of many kinds of sensors and control systems has been jolted into action in recent years. Tin dioxide (SnO_2) has been used as a gas sensor material to detect combustible and toxic gases such as CO, NH_3, NO_2, H_2S and CH_4. Commercial sensors typically use sintered SnO_2 powders, but thin films SnO_2 are gaining increasing popularity.[59,60] With the advent of advanced thin film technology more cost-effective, reproducible devices can be constructed with a reduction in device size and a concomitant increase in the speed of response by using SnO_2 thin films.

It is known that SnO_2 is used as a gas sensor because the number of electrons in the conduction band is affected by the adsorption of gaseous species on its surface.[61] Reducing gas molecules, such as CO, react with the oxygen species (O_2, O_2^-, O^-, and O) on the semiconductor surface.[62] This lowers the height of the Schottky barrier and increases the conductance of the material.[63,64] Gas sensors using

SnO_2 are widely used due to its high sensitivity to humidity and inflammable gases. In this type of sensors, gas concentration is related to the material's electrical impedance due to the adsorption of gas molecules on the SnO_2 surface. In a pure air environment, SnO_2 adsorbs oxygen that captures its electrons, thereby raising its resistivity. When a reducing gas is present, it competes for the adsorbed oxygen and hence the SnO_2 resistivity decreases. However, the electrical properties of SnO_2 are strongly dependent on material fabrication parameters. Since gas sensing is based on adsorption mechanisms on the SnO_2 grain surface, for high sensitivity a small grain size is desirable in order to achieve a high specific area, i.e. adsorption area per unit volume.[65,66]

The surface conductance of semiconducting oxide is affected by the concentration of ambient gases. Resistive gas sensors are based on this principle and the nature of the sensing mechanism is related to the electrical response of gas sensors to reactive gases. The change in the sensor resistance provides an indication of the gas concentration.[67] These sensors can be quite versatile as they may be used to detect oxygen, flammable gases and common toxic gases. Their mechanism of operation is complex, involving interactions between gaseous molecules and defects on the surface and grain boundaries. The sign of a change in resistance depends on whether the solid has *n*-type or *p*-type conductivity.[68,69] Structural properties such as grain size, grain geometry as well as specific surface area can significantly affect the gas sensing properties of semiconducting SnO_2. In order to control these structural characteristics, the microstructure evolution of SnO_2 thin films should be understood. Fractal method is a potentially powerful technique to characterize microstructures, and we are applying this technique to SnO_2 thin films for the first time in this study. Besides showing some examples of geometric structures of SnO_2 thin films, we shall discuss in detail the applicability and relevance of fractal theory to studying the microstructure and gas sensing behavior of SnO_2 based environmental functional materials. An integrated device for different gas species is highly desirable for versatile advanced applications. Despite the high sensitivity of SnO_2 to many gases, it is often susceptible to electrical drift

which requires long stabilization periods, as well as permanent poisoning after extended periods of operation. New fractal assessment strategies for this material formed at different substrate temperatures are of fundamental importance in the development of micro-devices.[70]

3.2. Fractal Assessment Strategies

In order to obtain the sintered SnO_2 target for pulsed laser deposition (PLD), we synthesized a pure nanocrystalline SnO_2 powder by the sol-gel method.[71] The fabrication method is described in the following. Meta-stannic acid sol (parent sol) was precipitated by treating a cold ethanol solution of $SnCl_4$ (27 %) with an aqueous ammonia solution (28 %) until a suitable pH value was reached. Dry powder with average grain size of about 4 nm was obtained by drying the parent sol, which had been washed repeatedly with de-ionized water. The SnO_2 discs, 15 mm in diameter and 4 mm in thickness, were prepared by compacting the powder under uniaxial pressure of 0.4 GPa, and sintered at 1150 ^{o}C for 2 h. The sintered disc consisted of high-purity cassiterite structure SnO_2 (99.8 %).

SnO_2 thin film was prepared by PLD techniques using the above sintered SnO_2 disc.[55] The target was cleaned with methanol in an ultrasonic cleaner before installation to minimize contamination. The laser was a KrF excimer laser (Lambda Physik, LEXtra 200, Germany) producing pulse energies of 350 mJ at a wavelength of 248 nm and a frequency of 10 Hz. The duration of every excimer laser pulse was 34 ns. The laser energy was transmitted onto the target in a high-vacuum chamber through an ultraviolet (UV)-grade fused silica window using an UV-grade fused silica lens. During the experiment, the target was kept rotating at a rate of 15 rpm to avoid drilling. The fluence was set at 5 J/cm^2 per pulse, corresponding to a total of approximately 1.5×10^5 laser pulses. The growth rate was estimated to be about 0.3 nm/s (or about 1 μm/h). The ablated substance was collected on a Si (100) substrate mounted on a substrate holder 4 cm away from the target. The high vacuum in the deposition chamber was

achieved by using a cryopump (Edwards Coolstar 800). The base pressure prior to laser ablation was about 1×10^{-6} mbar, and the oxygen partial pressure during laser ablation was set about 3×10^{-2} Pa. All deposition processes were carried out by in-situ operation on the substrate at temperatures of 300 ^{o}C, 350 ^{o}C, 400 ^{o}C, and 450 ^{o}C.

Scanning electron microscopy (SEM) images were digitized by using the Fractal Images Process Software (FIPS). These digitized images were divided into boxes of 360 × 360 size and then processed by the fractal theory.[72] Four intact fractal patterns were selected from these digitized images. The average value of the fractal dimensions (*D*), the fractal density and the average size of the fractal clusters for these digitized fractal patterns were obtained by using the box-counting method.[73] The carbon monoxide (CO) gas sensing property in the sensor was measured by a simple electrical measuring system. The test CO gas was introduced in the chamber by an injector with variable volume which facilitated control of gas concentration in the range 25-500 ppm. After the sensor was stabilized, the process was repeated by injecting a higher amount of the CO gas.

3.3. XRD and SEM Analysis

It is known that tin dioxide has a tetragonal rutile crystalline structure (known in its mineral form as cassiterite) with point group D_{4h}^{14} and space group $P4_2/mnm$. The unit cell consists of two metal atoms and four oxygen atoms. Each metal atom is situated amidst six oxygen atoms which approximately form the corners of a regular octahedron. Oxygen atoms are surrounded by three tin atoms which approximate the corners of an equilateral triangle. The lattice parameters are a = 4.7382(4) Å, and c = 3.1871(1) Å. Fig. 7A, B, C, and D show the XRD patterns of the SnO_2 thin films prepared on Si (100) substrate at 300 ^{o}C, 350 ^{o}C, 400 ^{o}C, and 450 ^{o}C respectively. The major diffraction peaks of some lattice planes can be indexed to the tetragonal unit cell structure of SnO_2 with lattice constants a = 4.738 Å and c = 3.187 Å, which are consistent with the standard values for bulk

SnO_2 (International Center for Diffraction Data (ICDD), PDF File No. 77-0447). The (hkl) peaks observed are (110), (101), (200), (211), (220), and (002). No characteristic peaks belonging to other tin oxide crystals or impurities were detected. The high intensity of these peaks suggests that these thin films mainly consist of the crystalline phase. As the substrate temperature increased, the crystallinity of the thin films was enhanced as manifested by the intensity and sharpness of the XRD peaks of the SnO_2 thin films. The substrate temperature dependence can be interpreted mainly by the mobility of the atoms in the thin films. At low substrate temperatures, the vapor species have a low surface mobility and are located at different positions on the surface. The low mobility of the species will prevent full crystallization of the thin films. However, at high substrate temperatures, the species with high enough mobility will arrange themselves at suitable positions in the crystalline cell.[74,75] The SnO_2 average grain sizes were calculated using the Scherrer formula: $D = K\lambda / \beta \cos\theta$, where D is the diameter of the nanoparticles, K = 0.9, λ (Cu K_α) = 1.5406 Å, and β is the full-width-at-half-maximum of the diffraction lines. The results show that the average grain sizes of the SnO_2 nanoparticles at different substrate temperatures are in the range of 25.3-27.8 nm. SnO_2 nanoparticle size increases from 25.3 nm at 300 °C to 26.2 nm at 350 °C. It then increases to 27.0 nm at 400 °C and finally to 27.8 nm at 450 °C. In fact, SnO_2 nanostructures can work as sensitive and selective chemical sensors. SnO_2 nanostructure sensor elements can be configured as resistors whose conductance can be modulated by charge transfer across the surface or as a barrier junction device whose properties can be controlled by applying a potential across the junction. Functionalizing the surface further offers a possibility to improve their sensing ability based on a better understanding of the influence of significant microstructural features, for example, the development of gas sensors for the detection of environmentally harmful gases.

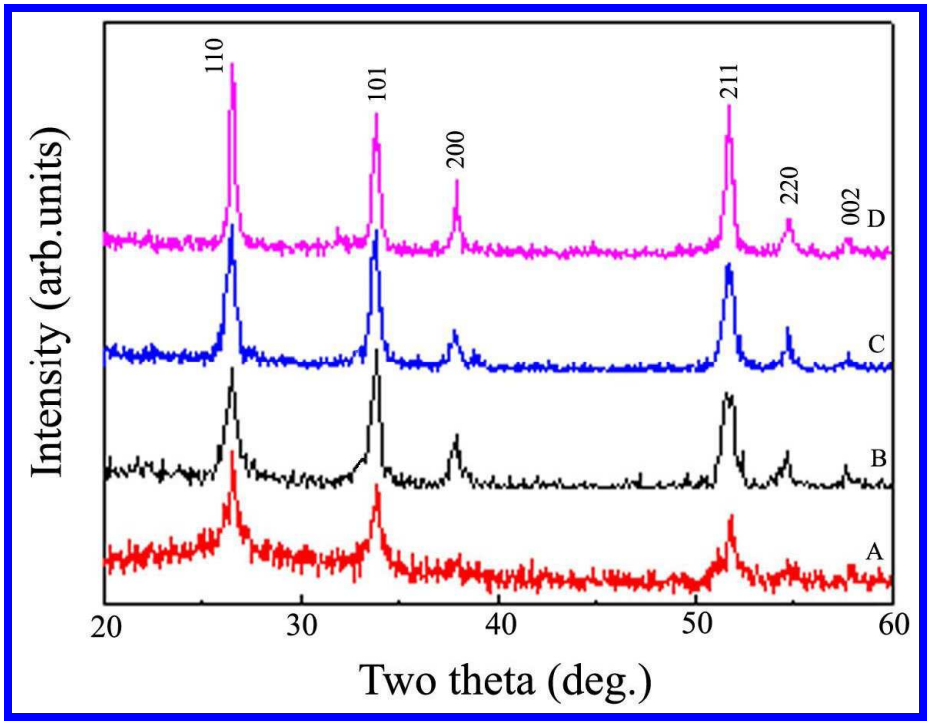

Fig. 7. XRD patterns of SnO_2 thin films prepared on Si (100) substrate at temperatures of (A) 300 ^{o}C; (B) 350 ^{o}C; (C) 400 ^{o}C; and (D) 450 ^{o}C.[70]

Fig. 8 presents SEM images of SnO_2 thin films prepared on Si (100) substrate at temperatures of (A) 300 ^{o}C, (B) 350 ^{o}C, (C) 400 ^{o}C, and (D) 450 ^{o}C respectively. The SEM observation indicated that all thin films produced under different substrate temperatures exhibited self-similar fractal patterns. It can be seen from Fig. 8 that the fractal patterns are open and loose structure with increasing substrate temperature. The average sizes of the fractal patterns (or clusters) are about 0.307 μm (see Fig. 8A), 0.906 μm (see Fig. 8B), 1.202 μm (see Fig. 8C) and 1.608 μm (see Fig. 8D). The average sizes of the fractal clusters for four thin films were estimated by measurement on the fractal regions. The measuring procedure is as follows: for each SEM image, we chose ten fractal patterns at random to get an average value. The average sizes of the fractal patterns were obtained by averaging the values of

SEM images with different orientations. It was found that the average sizes of the fractal clusters increase with increasing substrate temperature.

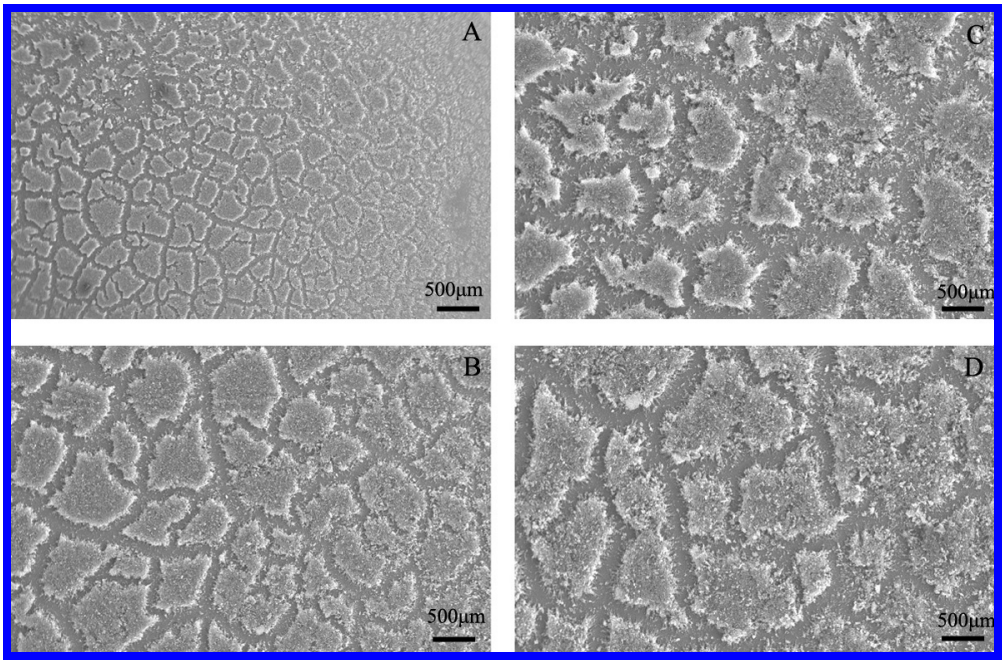

Fig. 8. SEM images of SnO_2 thin films prepared on Si (100) substrate at temperatures of (A) 300 ^{o}C; (B) 350 ^{o}C; (C) 400 ^{o}C; and (D) 450 ^{o}C.[70]

3.4. Fractal Dimension Calculation

Fig. 9 shows that the plots of ln(N) versus ln(1/L) of the fractal cluster regions in Fig. 8, where L is the box size and N is the number of boxes occupied by the SnO_2 clusters. It can be seen that all plots show good linearity, which means that the morphologies of SnO_2 clusters have scale invariance within these ranges. So the SnO_2 clusters can be regarded as fractals. In order to obtain the fractal dimension (D), we fit a linear relationship for the function ln(N) versus ln(1/L). The results show that the fractal dimension (D) is 1.896 at 300 ^{o}C as shown in Fig. 9A, 1.884 at 350 ^{o}C as shown in Fig. 9B, 1.865 at 400 ^{o}C as shown in Fig. 9C, and 1.818 at 450 ^{o}C as shown in Fig. 9D. We found that the fractal dimension (D) decreases with increasing substrate temperature. The smaller fractal dimension means

that the SnO_2 thin films are composed of the open and loose fractal structure with finer branches. Fig. 10A to C shows the distribution of the fractal average size, fractal dimension and fractal density for different substrate temperatures. It can be seen that there is an obvious increase in average fractal size (see Fig. 10A), and the fractal dimension generally decreases (see Fig. 10B) with increasing substrate temperature. In general, the fractal density is determined by the initial nucleation probability of the core crystal. From Fig. 10C, the fractal density was calculated to be 18, 6, 3, and 2 mm^{-2} at 300 ^{o}C, 350 ^{o}C, 400 ^{o}C, and 450 ^{o}C respectively. It was found that the fractal density gradually decreases with increasing substrate temperature. In the present work, the initial increase in nucleation probability was due to strain relaxation caused by the low short-range temperature field at 300 ^{o}C, so that the fractal density and their occupation area were high. With the increase of substrate temperature, the higher long-range temperature field may promote new nuclei and subsequent growth, which leads to the fractal growth of the fine branches and a lower fractal density. This fractal structure may lead to improvement in the design of gas sensors for the monitoring of environmental pollutants.

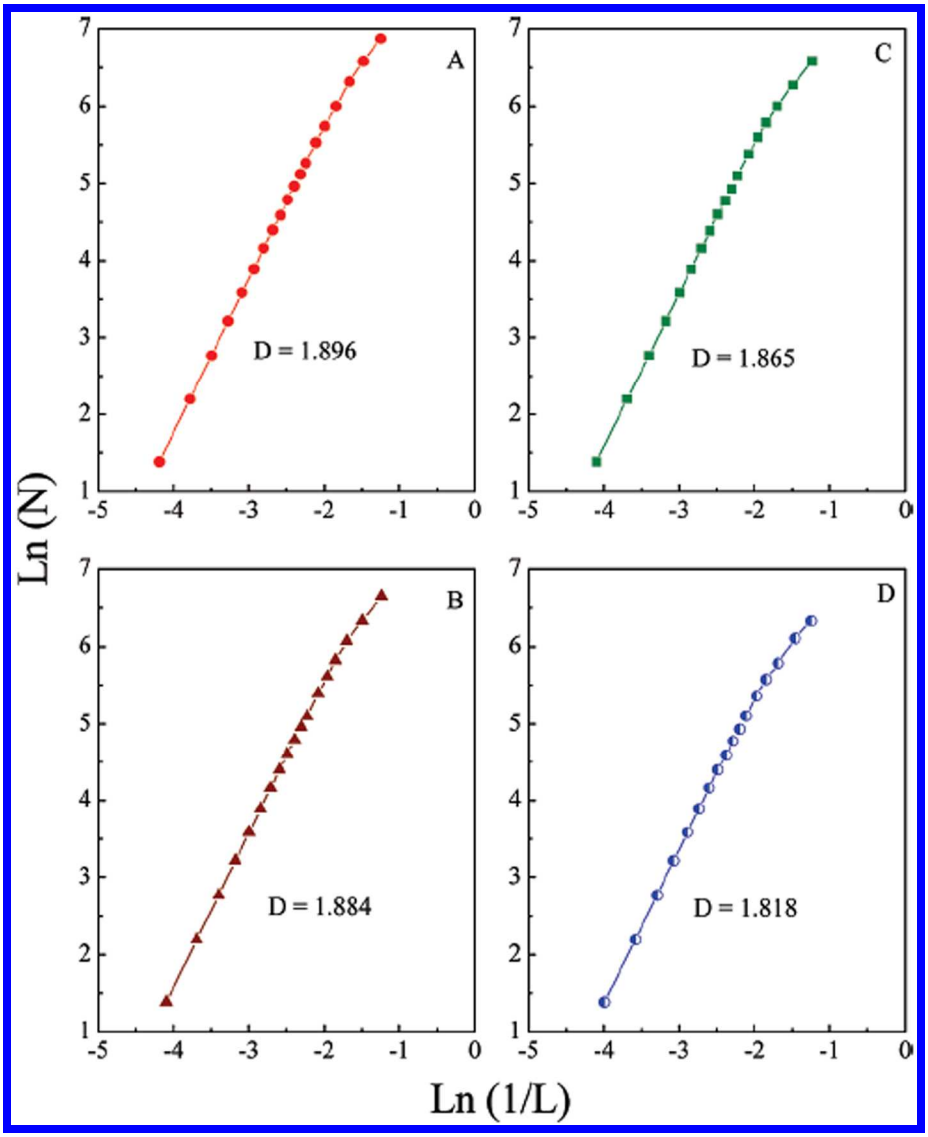

Fig. 9. Plots of ln(N) versus ln(1/L) of the fractal cluster regions in Fig. 3, where L is the box size and N is the number of boxes occupied by the SnO_2 crystalline structure for substrate temperatures at (A) 300 ^{o}C; (B) 350 ^{o}C; (C) 400 ^{o}C; and (D) 450 ^{o}C.[70]

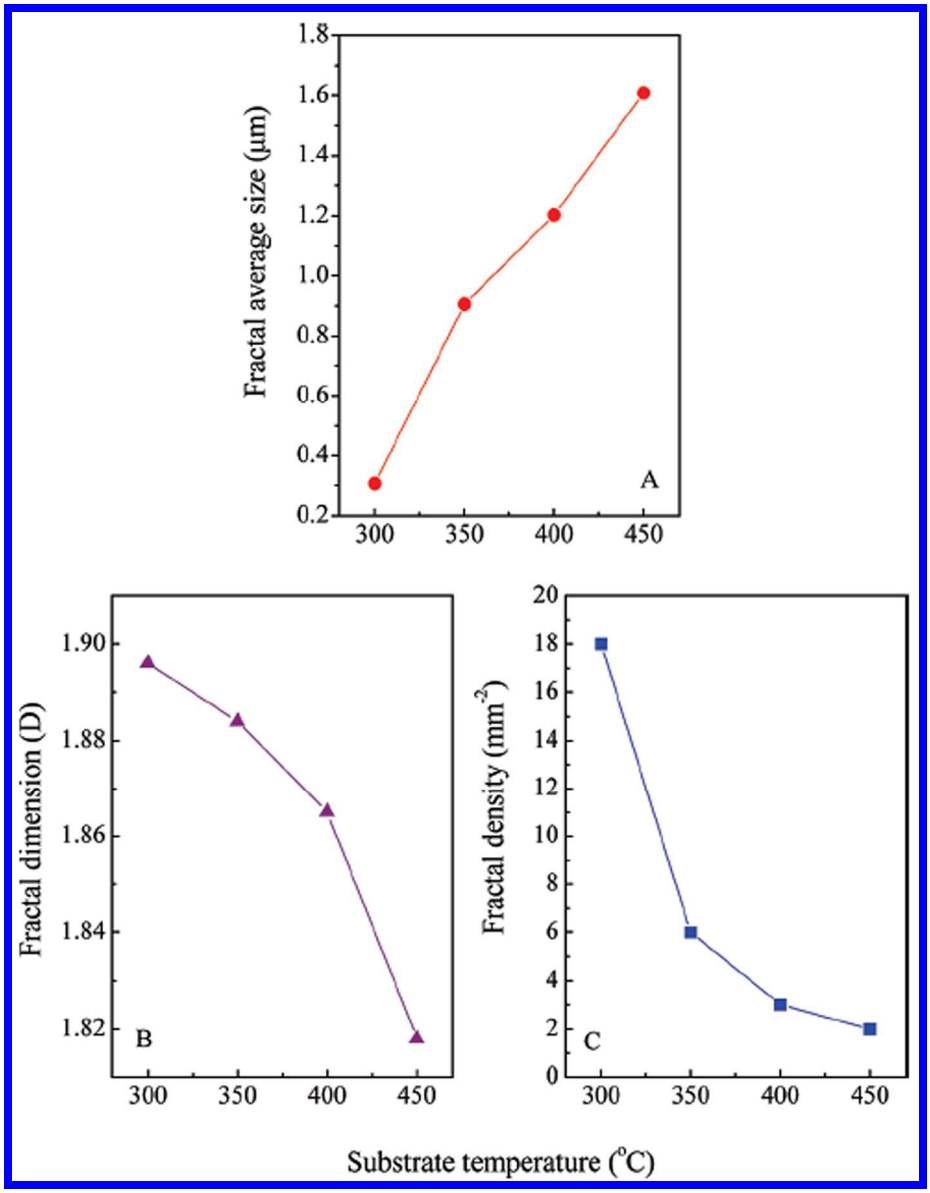

Fig. 10. (A) The fractal average size; (B) the fractal dimension; (C) the fractal density versus the substrate temperature.[70]

3.5. Fractal Formation Mechanism

On the basis of our experimental observation, the formation process of SnO_2 nanocrystals and fractal clusters could be reasonably described by a novel model, and be separated into eight steps, which illustrated in detail in Fig. 11.

(i) Operation of the KrF excimer laser at a repetition rate of 10 Hz at an incident angle of 45° to the polished sintered cassiterite SnO_2 target rotating at a rate of 15 rpm to avoid drilling.

(ii) Production of the high-temperature and high-pressure tin dioxide plasma at the solid-liquid interface quickly after the interaction between the pulsed laser and SnO_2 target.

(iii) Subsequent expansion of the high-temperature and high-pressure tin dioxide plasma leading to cooling of the tin dioxide plumes.[76-79] In our case, the interval between two successive pulses is much longer than the life of the plasma. Therefore, the next laser pulse had no interaction with the former plasma.

(iv) Deposition of the tin dioxide plume on the Si (100) substrate after the disappearance of the plasma, inducing the initial nucleation of SnO_2 nanocrystals.

(v) Grain rotation culminating in a low-energy configuration. This process is directly related to the reduction of surface energy, aimed at minimizing the area of high-energy interfaces.[45,46]

(vi) Possible formation of a coherent boundary between grains due to grain rotation, with the consequence of removing the common grain boundary and culminating in a single larger SnO_2 nanocrystal. This is the coalescence process.

(vii) Growth of SnO_2 nanocrystals along preferred crystallographic directions which could be predicted by an analysis of the surface energy in several crystallographic orientations.

(viii) Formation of the fractal structure as SnO_2 crystallizes and nucleates at high energy interfaces such as grains boundaries.

According to the fractal theory,[80,81] the heat released by crystallization leads to a local temperature rise in the surrounding area and this temperature field can propagate quickly and stimulate new nuclei appearing randomly in nearby regions. The stimulated nuclei of the next generation can also cause a

local temperature rise and repeat the above process many times until SnO_2 fractal patterns are formed. Based on the above proposed formation mechanism, we characterize the formation processes of SnO_2 nanocrystals and fractal structure in Fig. 11A-I. We believe that laser ablation technique is an appropriate method to synthesize a series of environmental functional materials with controlled composition, morphology and nanocrystal size, which are of important in the study of the sensitivity of SnO_2 thin films.

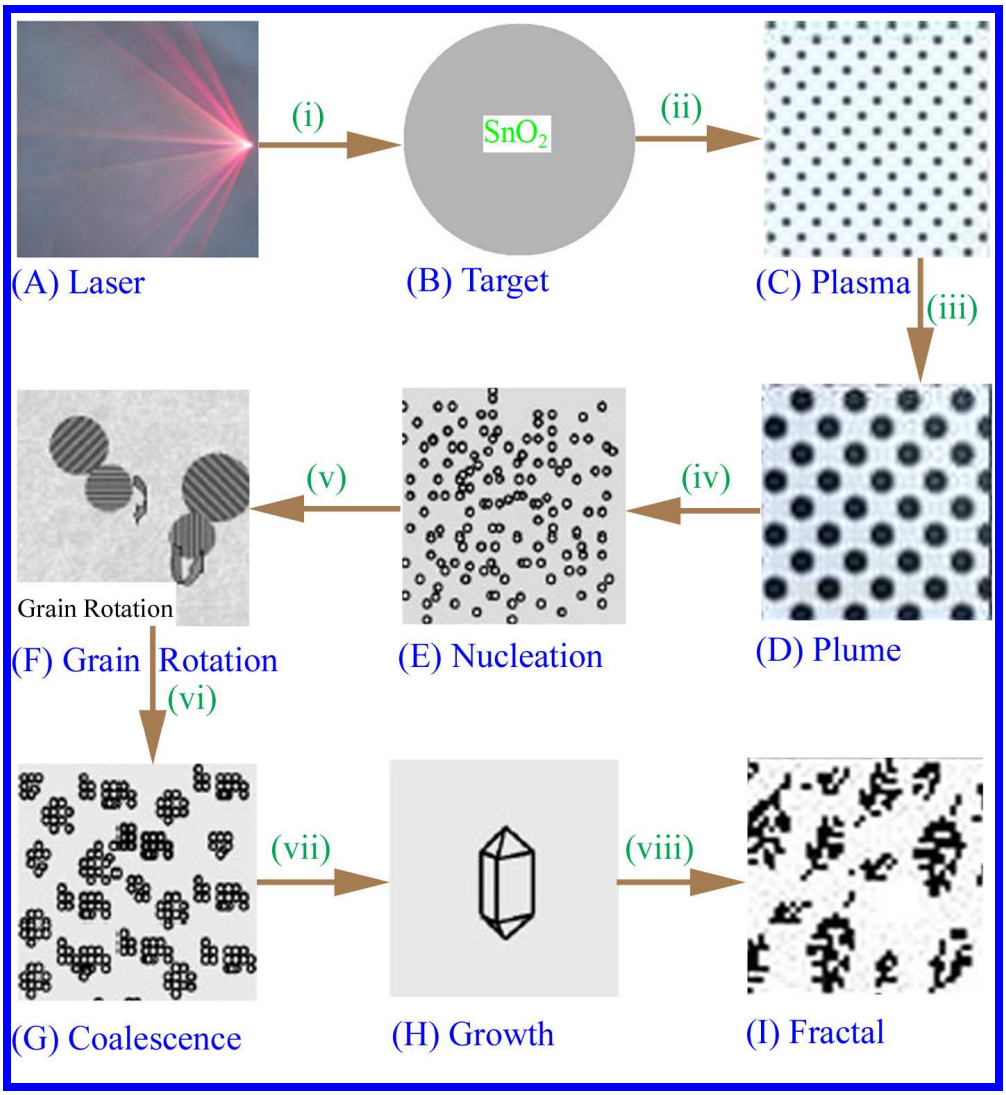

Fig. 11. The formation process of SnO_2 nanocrystals and fractal clusters. (A) Laser; (B) Target; (C) Plasma; (D) Plume; (E) Nucleation; (F) Grain Rotation; (G) Coalescence; (H) Growth; and (I) Fractal.[70]

3.6. Gas Sensing Behavior

To verify the gas sensing behavior of these SnO_2 thin films with interesting features of the fractal structure, we investigate the sensitivity dependence on carbon monoxide (CO) concentration, so as to achieve the aim of monitoring environmental pollutants. Fig. 12 shows the CO gas sensing behavior of the SnO_2 thin films prepared on Si (100) substrate at (A) 300 ^{o}C, (B) 350 ^{o}C, (C) 400 ^{o}C, and (D) 450 ^{o}C respectively. The measurement was performed at room temperature with CO concentrations of 25, 50, 75, 100, 200, 300, 400, and 500 ppm. We observe that the sensitivity increases with increasing CO concentration and substrate temperature. Similarly Cooper and Cicera found their SnO_2 thin film sensor possessed higher sensitivity to CO by using different procedures.[82,83] Further advancement of this gas sensor fabricated by the SnO_2 thin films with fractal structure to detect environmental harmful gases such as CO requires a clear understanding of its gas sensing mechanism. Our experimental results show that the CO gas sensing behavior clearly depends on the fractal dimension, fractal density, and average sizes of the fractal clusters (see Fig. 10 and 12). We propose a Random Tunneling Junction Network (RTJN) mechanism to explain this gas sensing behavior. After the fractal formation, the fractal clusters consist of the SnO_2 grains with the morphology of fine dendrite-like nanocrystals incorporating many tunneling junctions of varying sizes. From the view of electron transport, the whole thin film is made up of a series of tunneling junctions. For the SnO_2 thin films deposited at different substrate temperatures, the sizes of the fractal branches with different fractal dimensions are different, leading to differences in the height of the Schottky barrier of the tunneling junctions, with the consequence that the breakdown voltages are also different. During the measurement of the gas sensitivity, the reducing gas molecules such as CO react with the oxygen species (O_2, O_2^-, O^-, and O) ionized on the surface of the SnO_2 particles. This lowers the height of the Schottky barrier, and increases the conductance.[62-64] For example, for the SnO_2 thin film deposited at the lower substrate temperature (e.g. at 300 ^{o}C) with

the larger fractal dimension, the junction *i* will have the higher resistance state due to the thicker fractal branches, so the external voltage V_i cannot lower the Schottky barrier S_i and the junction *i* cannot be broken. The gas sensitivity is then lowered (see Fig. 12A). Conversely, for the SnO_2 thin film deposited at the higher substrate temperature (e.g. at 450 ^{o}C) with the smaller fractal dimension, the junction *i* will have the lower resistance state due to the finer fractal branches, so the external voltage V_i can lower the Schottky barrier S_i and the junction *i* will be broken. Therefore, the gas sensitivity would be higher (see Fig. 12D). As mentioned above, there is a relationship between the fractal dimension and the size of the fractal branches in that the number of the fine branches increases with decreasing fractal dimension. Therefore, the smaller the fractal dimension, the larger the number of junctions with the smaller Schottky barrier S_i and lower resistance state. The present findings reveal new opportunities for future study of fractal structure tin dioxide architectures, with the goal of optimizing environmental functional material properties for specific applications.

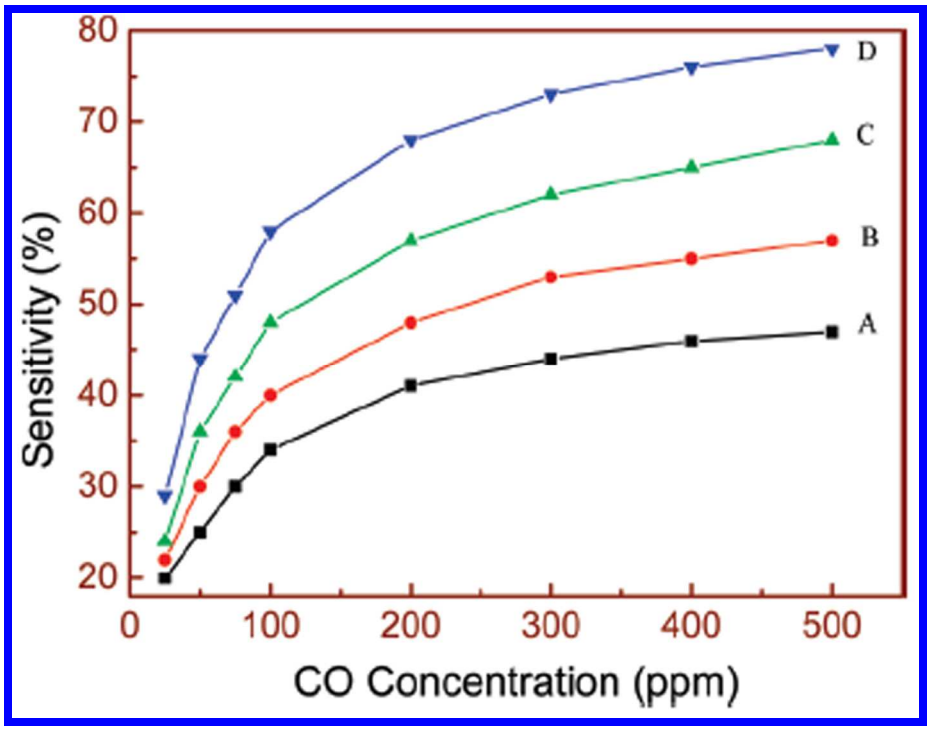

Fig. 12. The CO gas sensing behavior of SnO_2 thin films prepared on Si (100) substrate at temperatures of (A) 300 ^{o}C; (B) 350 ^{o}C; (C) 400 ^{o}C; and (D) 450 ^{o}C.[70]

4. Tin Dioxide Planted Graphene Nanosheets

4.1. Overview on Tin Dioxide Composite

Nanocomposites have attracted widespread attention because of their potential to combine desirable properties of different nanoscale building blocks to achieve advantageous electronic, optical, magnetic, and mechanic properties.[84-86] It has been demonstrated that the high-performance lightweight composites could be developed by dispersing strong and highly stiff fibres in a polymer matrix and tailored to individual applications.[87] Graphene as the basic plane of graphite is a single atomic layer of sp^2 hybridized carbon atoms arranged in a honeycomb lattice. Graphene materials have attracted special interest due to its excellent optical,[88-90] mechanical,[91-93] and electrochemical properties.[94-98] After an extensive search in the published literature, we stand at a similar threshold in the realm of incorporation of well-dispersed graphene-based sheets, produced by mechanical exfoliation, solution exfoliation and reduction of graphite oxide with metal oxides, to result in excellent applications. Many types of metal oxide/graphene nanocomposites have been effectively prepared and extensively discussed, including CoO/graphene,[99,100] Co_3O_4/graphene,[101-104] CuO/graphene,[105,106] Mn_3O_4/graphene,[107-109] Fe_3O_4/graphene,[110,111] NiO/graphene,[112] TiO_2/graphene,[113,114] and ZnO/graphene,[115] etc. These nanocomposites are achieved, not only by using the inherent properties of the nanofiller, but also more importantly by optimizing the dispersion, interface chemistry and nanoscale morphologies to take advantage of the enormous surface area per unit volume of graphene.

On the other hand, the size and morphology of metal oxides on graphene greatly affect their properties as well as their applications. For instance, when the size of the particle decreased, the surface-volume ratio and the band gap will increase correspondingly. This effect will finally lead to enhancement of the sensitivity of gas sensors.[70] Therefore, the quantum effects, particularly in size of quantum dots, have enhanced great interest in both basic and applied research.[38,116] However, most

metal oxide/graphene composites prepared so far have relatively larger sizes, over 10 nm up to hundreds of nanometers, with unsatisfactory dispersions. Furthermore, the main routes commonly used for the preparation of the metal oxide/graphene composites were either carried out with complicated processes or often suffered from poor manipulation on metal oxide/graphene composites. Therefore, it is highly desirable to develop a facile and general approach for the synthesis of metal oxide/graphene composites with favored microstructures for high-performance electrochemical properties.[117]

4.2. Tin Dioxide Planted Graphene Strategies

The reaction procedure can be described as a two-step method: (i) in situ loading of SnO_2 QDs (SQDs) onto graphene oxide (GO) and (ii) GO conversion to graphene. The detailed preparation procedure is as follows: GO solution was synthesized from natural graphite powders by a modified Hummer's method.[99] The GO was washed repeatedly with de-ionized water to completely remove metal and acid particles. SnO_2 quantum dots and graphene nanosheets (SQDs/GNS) composites were prepared by co-precipitation method of the GO and $SnCl_2 \cdot 2H_2O$ solution. In a typical synthesis, 100 ml GO solution was dispersed in 50 ml distilled water by ultrasonic treatment to form a colloidal suspension. Subsequently, the suspension was mixed with 10 ml aqueous solution of $SnCl_2 \cdot 2H_2O$ (0.45 g). The resulting mixture with the Sn/graphene ratio = 1:1 in weight was continually stirred for 30 min. The mixture was then placed in an ultrasonic bath for 60 min. The product was left for 24 h, washed completely with distilled water, and dried in vacuum at 60 ^{o}C. Finally, the product was annealed at 500 ^{o}C for 3 h in N_2 atmosphere. For comparison, the pure graphene nanosheets were prepared by the reduction of dried GO in N_2 atmosphere at 500 ^{o}C for 3 h.

The XRD patterns were obtained from a Japanese Regaku D/max-2500 machine using Cu K_α radiation in reflection geometry. An operating voltage of 40 kV and a current of 40 mA were used.

XRD patterns were recorded at a scanning rate of 0.08 $^{o}s^{-1}$ in the 2θ range 10 to 90°. Field emission-secondary electron microscopy (FE-SEM) imaging was carried out with a field emission scanning electron microanalyzer (JEOL-6700F, 15 kV). HRTEM observations were performed on a JEOL JEM-2010F electron microscope operating at 200 kV. Surface area determinations were performed by Brunauer-Emmett-Teller (BET) method using an ASAP-2000 Surface Area Analyzer (Micromeritics Instrument Corporation). Raman scattering measurements were obtained by backscattering geometry with a SPEX-1403 laser Raman spectrometer. The excitation source was an argon-ion laser operated at a wavelength of 514.5 nm in the backscattering configuration and a low incident power to avoid thermal effects. Thermogravimetric analysis (TGA) was conducted on a STA 449C instrument (Netzsch Instrument Co., German) from 30 to 1000 °C at a speed of 10 °C/min under N_2 atmosphere.

4.3. Microstructure Analysis

Fig. 13 shows the typical XRD patterns of (a) bare pure GNS, (b) SQDs/GNS composites, and (c) SnO_2 nanoparticles. The pure GNS only shows a strong (002) diffraction peak in the XRD pattern as shown in Fig. 13a. This peak shows that the GNS is multi-layer graphene stacked with an interlayer spacing of about 0.35 nm, indicating that the graphene is similar to natural graphene sheets (d_{002} = 0.34 nm).[118] Comparing Fig. 13a, b and c, it can be seen that the major diffraction peaks of some lattice planes of the SQDs/GNS composites as shown in Fig. 13b are similar to the tetragonal unit cell structure of SnO_2 with lattice constants a = 4.738 Å and c = 3.187 Å, consistent with the standard values for bulk SnO_2 (International Center for Diffraction Data (ICDD), PDF File No. 77-0447). The observed (*hkl*) peaks are (110), (101), (200), (211), (220), (002), (112) and (202), indicating that the SnO_2 particles in this composite are well-crystallized. The minor peak (particularly at ca. 15 degrees) belonging to other tin oxide crystals or impurities were detected. The high intensity of these peaks

suggests that this SQDs/GNS composite mainly consists of the crystalline phase, while the (002) diffraction peak of layered GNS has almost disappeared. Thus, we can speculate that the regular lamellar structure of the GNS sheets has been completely broken in the as-synthesized composites, forming exfoliated GNS nanosheets.

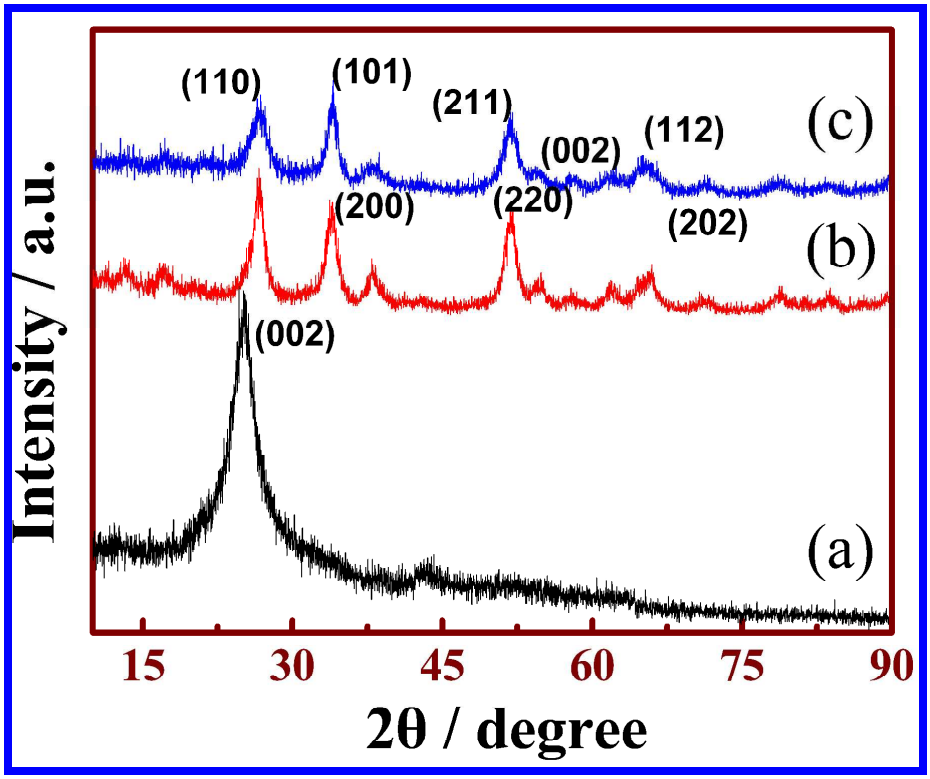

Fig. 13. The typical XRD patterns of (a) bare pure GNS, (b) SQDs/GNS composites, and (c) SnO_2 nanoparticles.[117]

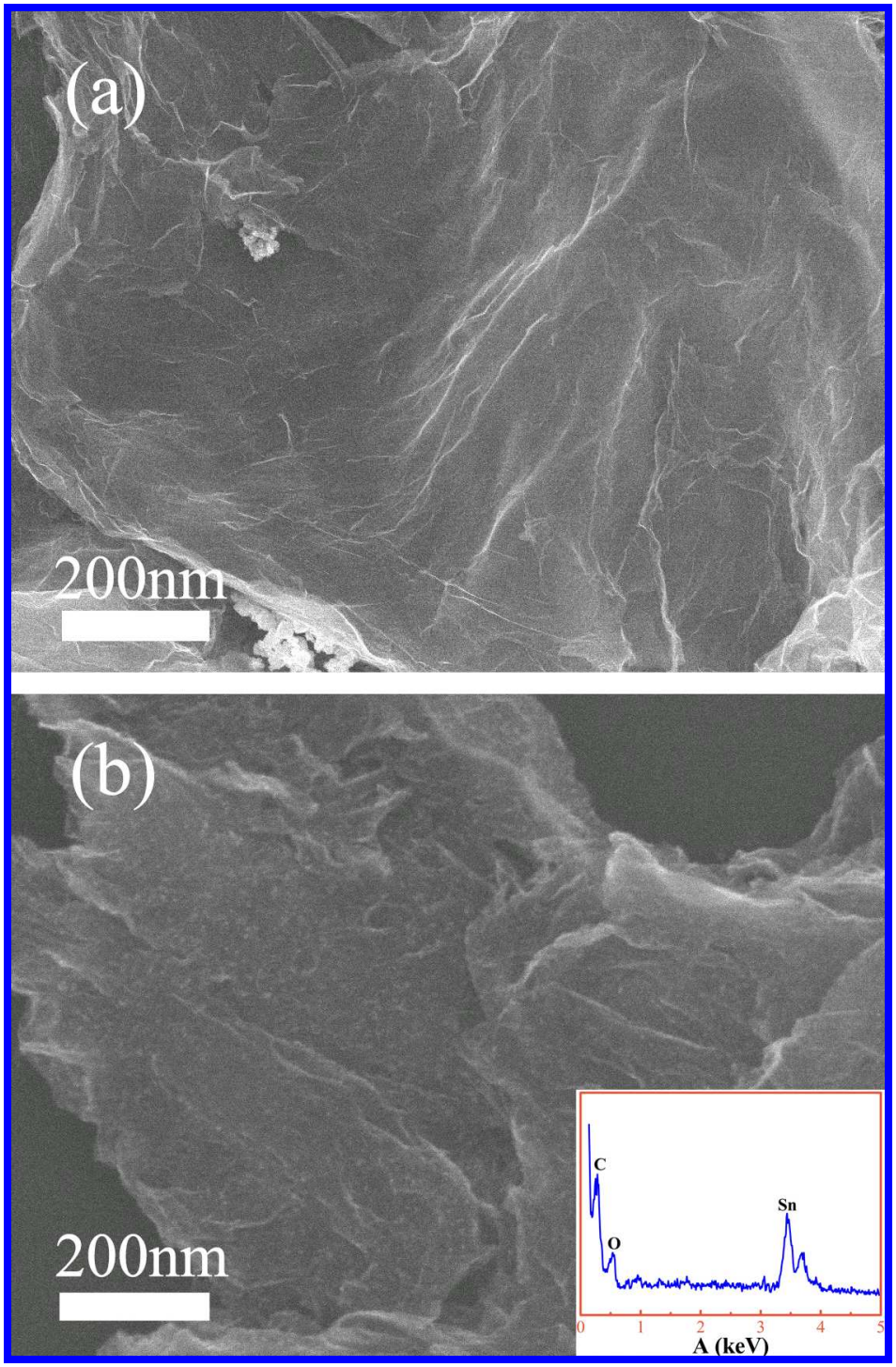

Fig. 14. FE-SEM images of (a) GNS and (b) SQDs/GNS composites on Si (100) substrates.[117]

Fig. 14 shows the FE-SEM images of (a) GNS and (b) SQDs/GNS composites on Si (100) substrates. Fig. 14a shows a representative SEM image of the GNS from the top view. This image shows layered platelets composed of curled nanosheets, in accordance with the (002) diffraction peak in the XRD pattern of the GNS. Fig. 14b shows the FE-SEM image of the SQDs/GNS composites prepared by the facile synthesis approach. It is found that the FE-SEM images of the GNS and SQDs/GNS composites have similar morphology, implying that a fine structural manipulation of the GNS was successfully achieved even after the reassembling process with SnO_2 nanoparticles. Interestingly, it can be seen clearly that the SnO_2 nanoparticles were uniformly distributed on the graphene nanosheets, by which graphene nanosheet restacking and SnO_2 nanoparticles aggregation were prevented. The component of prepared composites was confirmed by energy-dispersive X-ray analysis (EDS) as shown in the inset of Fig. 14b. It can be found that only Sn, C, and O elements were detected and the atomic ratio of Sn and C atoms was 1:10, which was consistent with their weight ratio (1:1). This further proves that the SnO_2 nanoparticles have been successfully assembled to the graphene nanosheets.

The surface morphology, particle size and microstructure of these SQDs/GNS composites were further investigated by HRTEM. Fig. 15a shows a typical exfoliated nanostructure. The TEM image clearly illustrates that the nanoparticles on the surface of the GNS were composed of homogeneous ultrafine SnO_2 nanoparticles. It is obvious that they can be called SnO_2 QDs which were uniformly distributed on the surface of the GNS in as-prepared SQDs/GNS composites. During the calcination process, the GNS distributed between SnO_2 QDs prevented the agglomeration of these SnO_2 nanoparticles,[119-121] which was of great benefit to the formation of SnO_2 QDs. The SnO_2 nanoparticles deposited on the GNS have also prevented the GNS from stacking into multi-layers[121-123] in accordance with the result that no obvious diffraction peak attributed to the GNS in the XRD pattern of the SQDs/GNS composites was observed. Fig. 15b displays a HRTEM image of the SQDs/GNS

composites. This shows clearly that the SnO_2 QDs can form in the SQDs/GNS composites. The size distribution of SnO_2 QDs is estimated to be a ranging from 4 to 6 nm and their average size is calculated to be about 4.8 ± 0.2 nm according to the XRD and HRTEM results. The clear lattice fringes demonstrate that the SnO_2 QDs were composed of ultrafine nanoparticles. In addition, the HRTEM image of a typical SnO_2 quantum dot shown in the inset of Fig. 15b proves that the clear crystal lattice with a spacing of 0.336 nm corresponds to (110) face of the SnO_2 rutile phase. Therefore, it is certain that the SnO_2 QDs distributed uniformly on the surface of the GNS were well-crystallized and was pure SnO_2. It is known that the embedding SnO_2 QDs in a graphene nanosheet matrix would be an ideal strategy to overcome the electrode material's poor cycling performance in lithium-ion batteries, which is attributed to the large volume changes and serious aggregation of particles during repeated lithium insertion and extraction reactions.[124] However, the synthesis of a single-layer graphene nanosheet matrix is very challenging due to its high surface energy.[125] Here, the SQDs/GNS composites with very few layers of graphene nanosheets have been successfully synthesized via a facile ultrasonic method. In addition, the approach is environmentally friendly because there is no toxic gas release during the reaction. Results show that this method can effectively prevent graphene nanosheets from being restacked, probably due to in situ loading of nanoparticles, which can decrease the surface energy of the graphene nanosheets.[124]

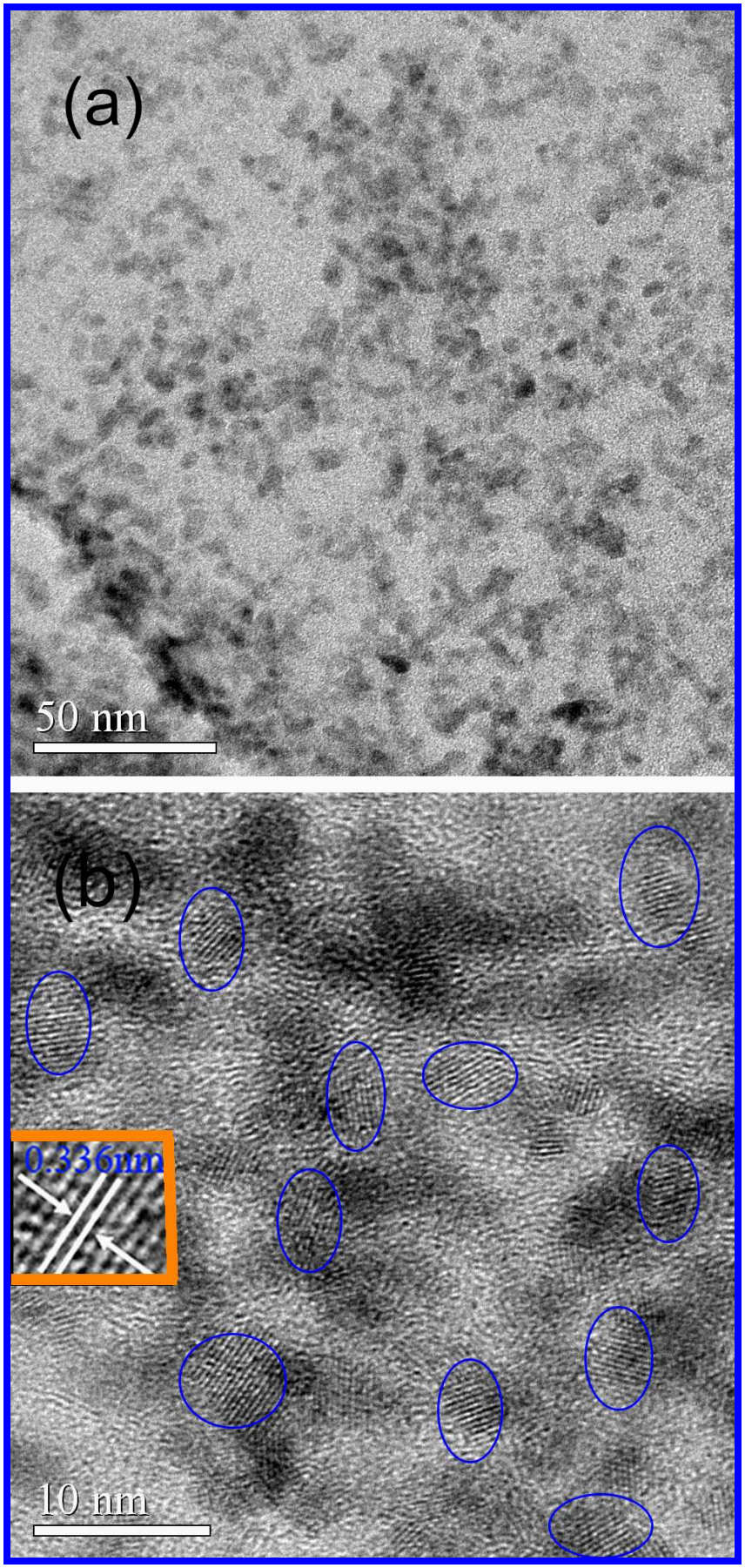

Fig. 15. TEM images of SQDs/GNS composites. (a) Low-magnification TEM image, (b) HRTEM image.[117]

In order to obtain further information on the microstructure evolution of chemical processing from GO to SQDs/GNS, Raman spectroscopy was employed owing to its fine sensitivity to the crystal surface. As seen in Fig. 16, the Raman spectrum of the GNS as shown in Fig. 16a contains both *D* band (~1335 cm^{-1}, k-point phonons of A_{1g} symmetry)[126] and *G* band (~1593 cm^{-1}, E_{2g} phonons of sp^2 atoms). Raman spectra with characteristic *D* and *G* bands are sensitive to detects, disorder and carbon grain size, and have been extensively used to characterize carbon materials. The *D* band in the Raman spectra is an indication of disorder in the GNS originating from defects associated with vacancies, grain boundaries, and amorphous carbon species. The Raman spectrum of SQDs/GNS composites as shown in Fig. 16b contains the *G* band at 1600.97 cm^{-1} owing to the presence of isolated double bonds that resonates at higher frequencies than the *G* band (1593.88 cm^{-1}) of the GNS. The I_D/I_G intensity ratio is a measure of the degree of disorder and average size of the sp^2 domains.[127-130] In Fig. 16, the I_D/I_G of the GNS is 1.09, but the value of I_D/I_G is 1.20 for the SQDs/GNS composites. Thus, there is an increased I_D/I_G intensity ratio in SQDs/GNS. When pyrolyzing GO to form GNS in N_2, the mass of GO sharply declined, accompanied by a large number of gas emissions, such as CO, CO_2 and H_2O. The graphene nanosheets are stripped by breaking the restraint of Van-Der-Waals force in this process.[131] The emission of CO and CO_2 results in a large loss of carbon atoms from the graphene layers. This generates a lot of carbon cavities, leading to disorder in pyrolyzed GNS. It is noticeable that an increased I_D/I_G ratio in SQDs/GNS (1.20) was observed in comparison with that of GNS (1.02) at the same annealing condition. This change suggests a decrease in the average size of the sp^2 domains,[132] and an increase in vacancies, grain boundaries, and amorphous carbon species. Because of the reduction effect of bivalent tin, the Sn^{2+} is integrated with the oxygen atom from the carboxy group of

GO to form SnO_2 nanoparticle during stirring and ultrasonic vibration. Therefore, the Raman results are consistent with the results of TEM and EDS, indicating the formation of SQDs/GNS composites.

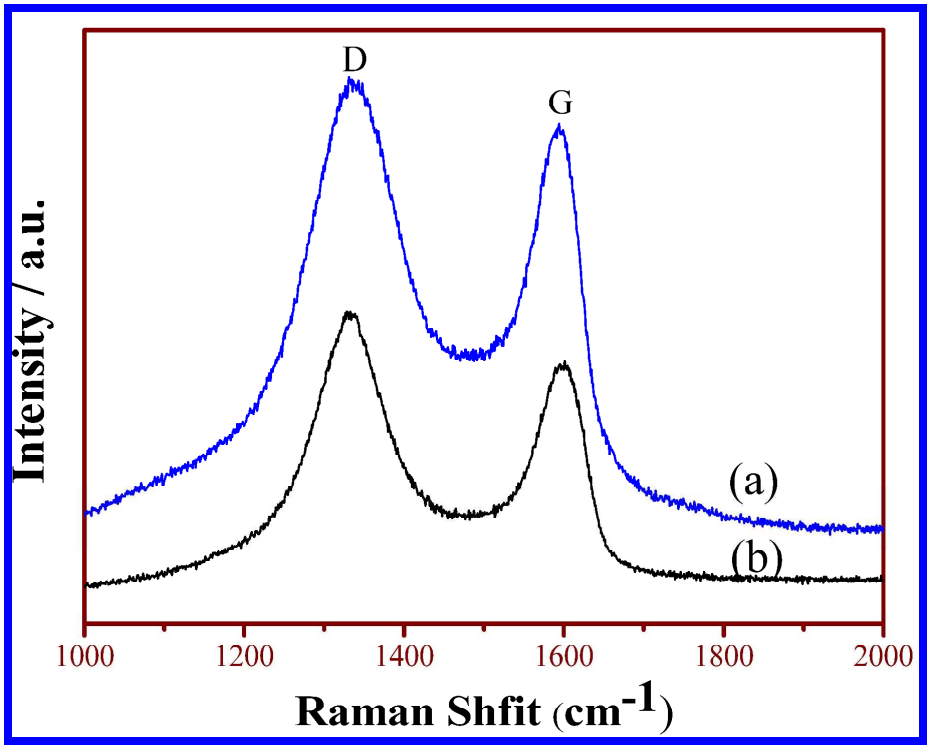

Fig. 16. Room-temperature Raman spectra of (a) GNS and (b) SQDs/GNS composites.[117]

4.4. BET Investigation

Thermoanalysis results of the pure GNS and SQDs/GNS composites are given in Fig. 17a and b respectively. As can be seen in Fig. 17, thermogravimetric (TG) analysis of the pure GNS shows that the amount of weight loss (mass loss ≈ 16.65%) is smaller than that of the SQDs/GNS composites (mass loss ≈ 26.27%). The redundant portion may be attributed to loss of ammonia, physically absorbed water, and chemically bonded water in the SnO_2 QDs.

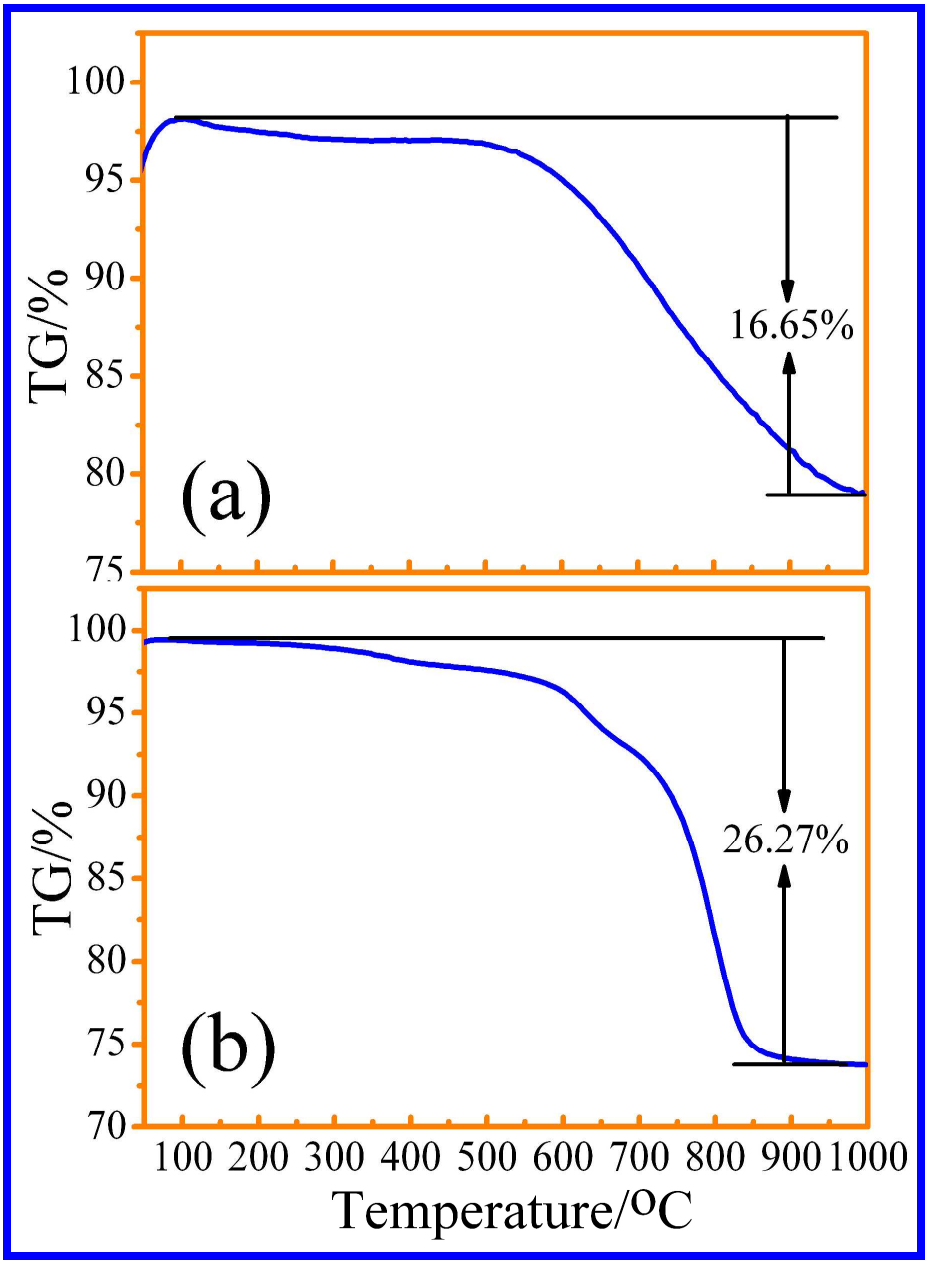

Fig. 17. TG curves of (a) GNS and (b) SQDs/GNS composites.[117]

N_2 adsorption/desorption isotherms were employed to investigate the pore structures of the GNS and SQDs/GNS composites as shown in Fig. 18a and b, respectively. The Brunauer-Emmett-Teller (BET) surface areas of the GNS and SQDs/GNS composites are about 205 m^2/g and 250 m^2/g, respectively. Obviously, the BET specific surface area of the SQDs/GNS composites is bigger than that of the GNS.

Because of the confinement effect of the GNS, the SnO_2 QDs can be separated one by one. Thus, the SnO_2 nanoparticles on the both sides of the GNS are expected to become smaller and the specific surface area of the SQDs/GNS composites became larger. A hysteresis loop in the nitrogen adsorption/desorption isotherms of the pure GNS was observed as shown in Fig. 18a, indicating that the graphene sheets are porous. This hysteresis loop resembles type-H3 IUPAC (International Union of Pure and Applied Chemistry) classification, and may result from slit-shaped pores between parallel layers.[133] However, a nitrogen sorption hysteresis loop in the SQDs/GNS composites was also clearly observed in Fig. 18b. The differences are that the adsorption branch rises slowly to the higher relative pressure point and then reaches to a constant value, whereas, the desorption branch moves slowly to middle P/P_0 signal point and decreases sharply, showing a clear type-H2 of the SQDs/GNS composites.[134] Furthermore, it should be pointed out that the nitrogen desorption of the SQDs/GNS composites occurs at much lower relative pressure than that of the GNS, indicating that desorption of N_2 molecules from the larger cavity is retarded by the smaller necks. For the above evidences, the ink-bottle-like pores structure can be concluded for the SQDs/GNS composites. For this structure, the desorption of N_2 occurs from the narrow neck and this is replenished from the larger parts of the pore.[135] Fig. 18c shows that the main pore size distribution of the GNS is about 3-5 nm, while Fig. 18d shows that the SQDs/GNS pore size distribution is between 2 and 4 nm. Interestingly, the GNS possesses higher porosity than that of the SQDs/GNS composites. The total pore volume of the GNS (0.47 cm^3g^{-1}) is larger than that of the SQDs/GNS composites (0.22 cm^3g^{-1}). It can be reasonably speculated that the decreased pore volume in the SQDs/GNS composites could arise primarily from the SnO_2 QDs, which filled the space of the close stacking of graphene nanosheets, consistent with the average size of 4.8 ± 0.2 nm for SnO_2 QDs in HRTEM observations as shown in Fig. 15b.

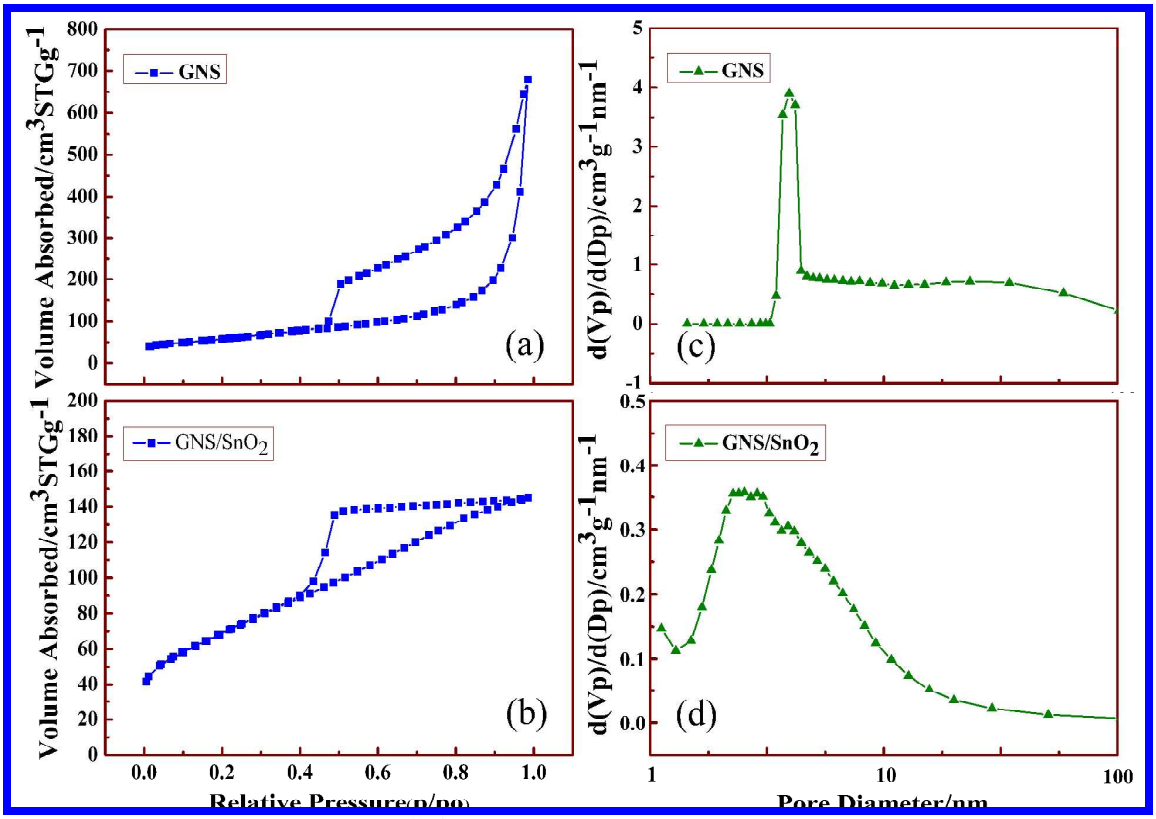

Fig. 18. Nitrogen adsorption/desorption isotherms of (a) GNS and (b) SQDs/GNS composites. Pore diameter distribution patterns of (c) GNS and (d) SQDs/GNS composites.[117]

4.5. Formation Mechanism

Further development of the SQDs/GNS composites requires a clear understanding of their formation mechanism. On the basis of our experimental results, Fig. 19 shows the formation processes of the SQDs/GNS composites, which could be reasonably described by a novel model, and be separated into three steps. A GO sheets solution is fabricated from pristine graphite. Many previous studies have confirmed that the GO sheets are heavily oxygenated with hydroxyl and epoxide functions groups decorated on their basal planes, in addition to carbonyl and carboxyl groups located at the sheets edges.[133,136] Firstly, the GO was well dispersed in distilled water to form a uniform GO nanosheets suspension by the strong hydrophilic of these functional groups.[121,137] Then, the GO solution was

mixed with a certain concentration $SnCl_2$ solution. Sn^{2+} ion is selectively bonded with carboxyl and carbonyl through electrostatic attraction.[138] As a result of the strong stirring conditions, the mixture solution is homogeneously dispersed and Sn^{2+} ions are also uniformly dispersed on the surface of GO sheets. Under ultrasonic vibration conditions, the interlayer spacing gradually increases, and Sn^{2+} ions could easily migrate into the enlarged layer. Then Sn^{2+} ions, which are adsorbed firmly on the both sides of the GO, prohibit the stacking of the GO by Van Der Waals forces. Sn^{2+} ions are not very stable due to electrostatic attraction. Finally, the precursor is heated at 500 ^{o}C in N_2 for 3 h. The basic Sn^{2+} ions should be converted uniformly to small SnO_2 QDs and the reduction of the GO. The GNS should occur simultaneously. We think that the rational selection of the $SnCl_2$ precursor and the ultrasonic method may be critical for the successful preparation of uniformly dispersed SnO_2 QDs on graphene substrates. First, the basic Sn^{2+} ions are firmly anchored on both sides of the GO through electrostatic attraction, and thus enhance the conjunction stability of the hybrids. This is an essential way to get the highly dispersed Sn^{2+} ions on the GNS. Subsequently, the ultrasonic method provides a necessary driving force for complete uniform disposition.

To sum up, we have reported a facile one-step ultrasonic way to synthesize SnO_2 QDs on graphene nanosheets by using $SnCl_2{\cdot}2H_2O$ as a precursor at ambient temperature. We believe that the incorporation of well-dispersed graphene-based nanosheets with the metal oxides was an effective way to achieve the SnO_2 nucleation and the SnO_2 QDs growth. In this article, we provided some preliminary investigations in assembling SnO_2 QDs to graphene nanosheets. The further detailed investigations on the influence some specific synthetic conditions (such as Sn:GO ratio, calcination temperature, sonication time, and pH value of the solution) on the experimental results are in progress. The ultrasonic process indicated that the loading of SnO_2 QDs was an effective way to prevent graphene nanosheets from being restacked during the reduction. The calcination process revealed that the graphene nanosheets distributed between SnO_2 nanoparticles also prevented the agglomeration of SnO_2

nanoparticles, which were beneficial to the formation of SnO_2 QDs. The present results indicated that this research has carried out important developments to the SnO_2/graphene nanocomposites.

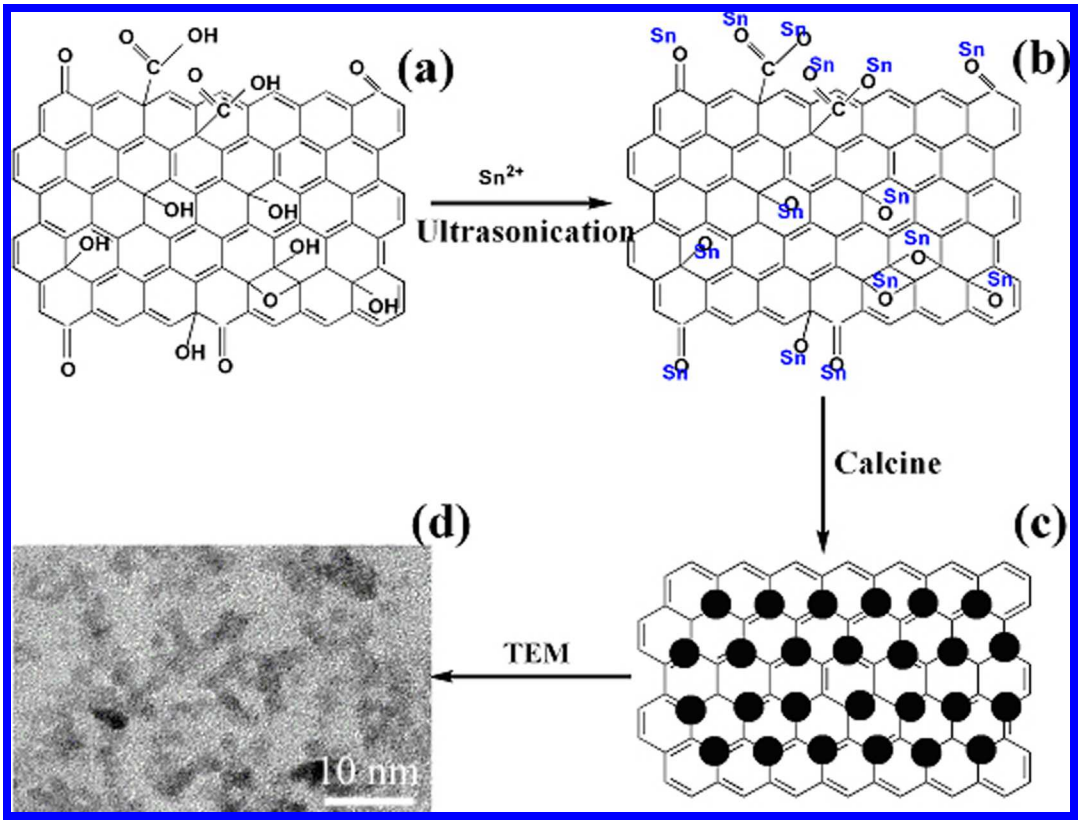

Fig. 19. Schematic formation mechanism of SQDs/GNS composites. (a) GO, (b) electrostatic interaction between oxide functional groups of GO and Sn^{2+}, (c) graphene decorated with SnO_2 nanoparticles (filled circles) after the calcine treatment, and (d) TEM image of SQDs/GNS composites.[117]

5. Conclusion and Outlook

5.1. Conclusion

In this article, we has reviewed the efforts toward understanding the synthesis strategies, microstructual evolution, related formation mechanism, and performance evaluation of SnO_2 various

morphologies including SnO_2 QDs, thin films, and composites prepared by electron-beam irradiation, pulsed laser ablation, and SnO_2 planted graphene strategies. The following conclusions can be drawn from the present work:

In the section 2, the electron-beam irradiation strategies for growth behavior of SnO_2 nanocrystals were assessed in detail. It can be emphasized that the crystallinity of irradiated SnO_2 powders is better than unirradiated one. The BET specific surface area of the irradiated sample is much higher, which is almost doubled at 1400 kGy. The appearance of new Raman peaks is closely related to the relaxation of Raman selection rule due to the EBI effects in the increasing of QD density and high concentration of defects in surface site. Under 1400 kGy irradiation dose, the high-quality of SnO_2 QDs with diameter ranging from 2 to 4 nm can be obtained. The clear lattice fringes of the QDs indicated that the crystal planes of the QDs are structurally perfect and uniform. Slight misorientations changing in the QD orientation demonstrated that the grain boundary must migrate toward the smaller crystal nucleus, resulting in a single larger QD. The results revealed that the electron-beam irradiation method is a potentially powerful technique to achieve SnO_2 nucleation and QD growth.

In the section 3, SnO_2 thin films prepared at different substrate temperature with interesting fractal features were presented. The experimental evidence indicated that the fractal clusters with various sizes, densities, and fractal dimensions were affected by different substrate temperature. The formation of significant fractal features was described by (i) operation of the KrF excimer laser; (ii) production of the tin dioxide plasma; (iii) cooling of the tin dioxide plumes; (iv) deposition of the tin dioxide plume on the Si substrate; (v) grain rotation; (vi) formation of coherent boundary between grains followed by coalescence; (vii) growth of SnO_2 nanocrystals along preferred crystallographic directions; and (viii) formation of the fractal structure. The CO gas sensing behavior was sensitively dependent on fractal dimensions, fractal densities, and average sizes of the fractal clusters. The sensitivity increases with

increasing CO concentration and decreasing fractal dimension. The Random Tunneling Junction Network (RTJN) mechanism can be applied to explain this gas sensing behavior.

In the section 4, a ultrasonic approach for the facile synthesis of SQDs/GNS composites using GO as supporting materials and $SnCl_2$ as a precursor was presented in detail. The microstructural analysis indicated that the GNS was exfoliated and decorated with SnO_2 QDs, which was dispersed uniformly on both sides of the graphene. The size distribution of SnO_2 QDs was estimated to be a ranging from 4 to 6 nm and their average size was calculated to be about 4.8 ± 0.2 nm. The clear lattice fringes of SQDs indicated that the crystal planes of SQDs were structurally perfect and uniform. Investigations of Raman spectra showed that the SQDs/GNS composites contained both *D* band and *G* band. The increased I_D/I_G intensity ratio in SQDs/GNS composites was closely related to the SQDs on the GNS. The BET specific surface area (250 m^2/g) of the SQDs/GNS was higher than that of the GNS (205 m^2/g). The results revealed that the incorporation of well-dispersed graphene-based sheets with metal oxide is an effective way to achieve the SnO_2 nucleation and SnO_2 QD growth.

5.2. Outlook

In fact, the rise of low dimensional SnO_2 nanostructured materials has opened up new routes for their use in various materials engineering applications. Significant impacts have also been made along the way. Of course, investigation in the SnO_2 based applications still poses many critical problems that need to be addressed and understood. In particular, these crucial problems include:

(i) Development of improved methods of structurally controlled growth of semiconductor SnO_2 nanomaterials based on adjustment of structural parameters. For example, the electron-beam irradiation techniques should be further applied to the preparation and modification of materials.

(ii) Challenging issue for future research in the field of the fractal semiconductors is the fabrication of the related advanced controllable micro/nanostructures with novel and improved properties. Most surface, interface, and quantum structures can be good functional parts of advanced applications. For example, the formation processes of SnO_2 nanocrystals and fractal clusters can be reasonably described by the fractal theory.

(iii) Achievement of better understanding of the interaction between low-dimensional SnO_2-based nanomaterials and other elemental species arising from the process of doping, modification, and formation of composites, and associated micro/nanostructure changes caused by composition modulation. For example, the incorporation of well-dispersed graphene-based nanosheets with metal oxide is an effective way to achieve the nucleation and growth of the metal oxide nanocrystals and quantum dots.

There is still a lot of room for development in semiconductor SnO_2 nanomaterials to realize its full potential. Future work in this field should focus on the above mentioned areas to enable commercial SnO_2 micro/nanodevices to be available for practical applications.

Acknowledgements

The work described in this article was financially supported by the National Natural Science Foundation of China (Project Numbers: 11375111, 11428410 and 11074161) , the Research Fund for the Doctoral Program of Higher Education of China (Project Number: 20133108110021), the Key Innovation Fund of Shanghai Municipal Education Commission (Project Numbers: 14ZZ098 and 10ZZ64), the Science and Technology Commission of Shanghai Municipality (Project Numbers: 14JC1402000 and 10JC1405400), the Shanghai Pujiang Program (Project Number: 10PJ1404100), and the Program for Innovative Research Team in University (Project Number: IRT13078). This work was

also supported by a General Research Fund from the Research Grants Council, Hong Kong (Project Number: CityU 119212).

Notes and references

(1) Z. W. Chen, J. K. L. Lai and C. H. Shek, *Chem. Phys. Lett.*, 2006, **422**, 1.

(2) L. P. Qin, J. Q. Xu, X. W. Dong, Q. Y. Pan, Z. X. Cheng, Q. Xiang and F. Li, *Nanotechnology*, 2008, **19**, 185705.

(3) Z. W. Chen, J. K. L. Lai and C. H. Shek, *J. Non-Cryst. Solids*, 2005, **351**, 3619.

(4) Z. W. Chen, J. K. L. Lai and C. H. Shek, *Phys. Lett. A*, 2005, **345**, 391.

(5) Z. W. Chen, Z. Jiao, D. Y. Pan, Z. Li, M. H. Wu, C. H. Shek, C. M. L. Wu and J. K. L. Lai, *Chem. Rev.*, 2012, **112**, 3833.

(6) J. Du, J. Wang, Z. Jiao, M. H. Wu, C. H. Shek, C. M. L. Wu, J. K. L. Lai and Z. W. Chen, *J. Nanosci. Nanotechnol.*, 2011, **11**, 9709.

(7) Z. W. Chen, Q. B. Li, D. Y. Pan, Z. Li, Z. Jiao, M. H. Wu, C. H. Shek, C. M. L. Wu and J. K. L. Lai, *J. Phys. Chem. C*, 2011, **115**, 9871.

(8) Z. Ying, Q. Wan, Z. T. Song and S. L. Feng, *Nanotechnology*, 2004, **15**, 1682.

(9) P. C. Pandey, B. C. Upadhyay, C. M. D. Pandey and H. C. Pathak, *Sens. Actuators B*, 1999, **56**, 112.

(10) W. A. Badawy, *Sol. Energy Mater. Sol. Cells*, 2002, **71**, 281.

(11) Y. S. Cho, G. R. Yi, J. J. Hong, S. H. Jang and S. M. Yang, *Thin Solid Films*, 2006, **515**, 1864.

(12) F. Gu, S. F. Wang, H. M. Cao and C. Z. Li, *Nanotechnology*, 2008, **19**, 095708.

(13) Z. R. Dai, Z. W. Pan and Z. L. Wang, *Adv. Funct. Mater.*, 2003, **13**, 9.

(14) X. Wang, J. Zhuang, Q. Peng and Y. D. Li, *Nature*, 2005, **437**, 121.

(15) G. R. Patzke, F. Krumeich and R. Nesper, *Angew. Chem. Int. Ed.*, 2002, **41**, 2446.

(16) Y. Xia, Y. J. Xiong, B. Lim and S. E. Skrabalak, *Angew. Chem. Int. Ed.*, 2009, **48**, 60.

(17) Y. Yin and A. P. Alivisatos, *Nature*, 2005, **437**, 664.

(18) Y. Shimizu, A. Jono, T. Hyodo and M. Egashira, *Sens. Actuators B*, 2005, **108**, 56.

(19) X. W. Lou, L. A. Archer and Z. Yang, *Adv. Mater.*, 2008, **20**, 3987.

(20) Z. W. Chen, C. M. L. Wu, C. H. Shek, J. K. L. Lai, Z. Jiao and M. H. Wu, *Crit. Rev. Solid State Mater. Sci.*, 2008, **33**, 197.

(21) Z. Ying, Q. Wan, Z. T. Song and S. L. Feng, *Nanotechnology*, 2004, **15**, 1682.

(22) P. C. Pandey, B. C. Upadhyay, C. M. D. Pandey and H. C. Pathak, *Sens. Actuators B*, 1999, **56**, 112.

(23) W. A. Badawy, *J. Alloys Compd.*, 2008, **464**, 347.

(24) Y. S. Cho, G. R. Yi, J. J. Hong, S. H. Jang and S. M. Yang, *Thin Solid Films*, 2006, **515**, 1864.

(25) F. Gu, S. F. Wang, H. M. Cao and C. Z. Li, *Nanotechnology*, 2008, **19**, 095708.

(26) L. Kőrösi, S. Papp, V. Meynen, P. Cool, E. F. Vansant and I. Dékány, *Colloids Surf. A*, 2005, **268**, 147.

(27) Y. Liu, E. Koep and M. Liu, *Chem. Mater.*, 2005, **17**, 3997.

(28) F. Paraguay-Delgado, W. Antúnez-Flores, M. Miki-Yoshida, A. Aguilar-Elguezabal, P. Santiago, R. Diaz and J. A. Ascencio, *Nanotechnology*, 2005, **16**, 688.

(29) B. Cheng, J. M. Russell, W. S. Shi, L. Zhang and E. T. Samulski, *J. Am. Chem. Soc.*, 2004, **126**, 5972.

(30) T. Krishnakumar, R. Jayaprakash, M. Parthibavarman, A. R. Phani, V. N. Singh and B. R. Mehta, *Mater. Lett.*, 2009, **63**, 896.

(31) G. C. Xi and J. H. Ye, *Inorg. Chem.*, 2010, **49**, 2302.

(32) E. J. H. Lee, C. Ribeiro, T. R. Giraldi, E. Longo, E. R. Leite and J. A. Varela, *Appl. Phys. Lett.*, 2004, **84**, 1745.

(33) Z. W. Chen, J. K. L. Lai and C. H. Shek, *Appl. Phys. Lett.*, 2006, **88**, 033115.

(34) H. L. Zhu, D. R. Yang, G. X. Yu, H. Zhang and K. H. Yao, *Nanotechnology*, 2006, **17**, 2386.

(35) J. D. Castillo, V. D. Rodríguez, A. C. Yanes, J. Méndez-Ramos and M. E. Torres, *Nanotechnology*, 2005, **16**, S300.

(36) H. M. Dahlan, M. D. Khairul Zaman and A. Ibrahim, *Radiat. Phys. Chem.*, 2002, **64**, 429.

(37) Z. Li, Z. Jiao, M. H. Wu, Q. Liu, H. J. Zhong and X. Geng, *Colloids Surf. A*, 2008, **313**, 40.

(38) J. Wang, J. Du, C. Chen, Z. Li, Z. Jiao, M. H. Wu, C. H. Shek, C. M. L. Wu, J. K. L. Lai and Z. W. Chen, *J. Phys. Chem. C*, 2011, **115**, 20523.

(39) Z. M. Jarzebski and J. P. Marton, *J. Electrochem. Soc.*, 1976, **123**, 199C.

(40) Z. W. Chen, J. K. L. Lai, C. H. Shek and H. D. Chen, *Appl. Phys. A*, 2005, **81**, 959.

(41) B. D. Cullity, *Elements of X-ray Diffractions*, Addition-Wesley: MA, 1978.

(42) Y. J. Lin and C. J. Wu, *Surf. Coat. Technol.*, 1996, **88**, 239.

(43) J. J. Zhu, J. M. Zhu, X. H. Liao, J. L. Fang, M. G. Zhou and H. Y. Chen, *Mater. Lett.*, 2002, **53**, 12.

(44) Y. F. Zeng, Z. L. Liu and Z. Z. Qin, *J. Hazard. Mater.*, 2009, **162**, 682.

(45) R. L. Penn and J. F. Banfield, *Geochim. Cosmochim. Acta*, 1999, **63**, 1549.

(46) R. L. Penn and J. F. Banfield, *Science*, 1998, **281**, 969.

(47) A. Diéguez, A. Romano-Rodríguez, A. Vilà and J. R. Morante, *J. Appl. Phys.*, 2001, **90**, 1550.

(48) W. Z. Wang, C. K. Xu, G. H. Wang, Y. K. Liu and C. L. Zheng, *J. Appl. Phys*., 2002, **92**, 2740.

(49) S. H. Sun, G. W. Meng, G. X. Zhang, T. Gao, B. Y. Geng, L. D. Zhang and J. Zuo, *Chem. Phys. Lett.*, 2003, **376**, 103.

(50) Y. J. Jiang, L. J. Liao, G. Chen and P. X. Zhang, *Phys. Stat. Sol. B*, 1989, **156**, 145.

(51) L. Abello, B. Bochu, A. Gaskov, S. Koudryavtseva, G. Lucazeau and M. Roumvantesva, *J. Solid State Chem.*, 1998, **135**, 78.

(52) K. N. Yu, Y. H. Xiong, C. S. Xiong, Y. T. Qian and Y. Hu, *NanoStruct. Mater.,* 1995, **5***,* 819.

(53) Z. L. Wang and Z. C. Kang, *Functional and Smart Materials-Structural Evolution and Structure Analysis*, Plenum Press, New York, 1998.

(54) Z. W. Pan, Z. R. Dai and Z. L. Wang, *Science*, 2001, **291**, 1947.

(55) Z. W. Chen, J. K. L. Lai and C. H. Shek, *Phys. Rev. B*, 2004, **70**, 165314.

(56) Z. R. Dai, J. L. Gole, J. D. Stout and Z. L. Wang, *J. Phys. Chem. B*, 2002, **106**, 1274.

(57) Z. L. Wang, *Adv. Mater.*, 2003, **15**, 432.

(58) H. T. Ng, J. Li, M. K. Smith, P. Nguyen, A. Cassell, J. Han and M. Meyyappan, *Science*, 2003, **300**, 1249.

(59) U. Mikko, L. Hanna, V. Heli, N. Lauri, R. Resch and F. Gernot, *Mikrochim. Acta*, 2000, **133**, 119.

(60) P. Hidalgo Falla, H. E. M. Peres, D. Gouvêa and F. J. Ramirez-Fernandez, *Mater. Sci. Forum*, 2005, **498-499**, 636.

(61) T. Oyabu, *J. Appl. Phys.*, 1982, **53**, 2785.

(62) Z. W. Chen, J. K. L. Lai and C. H. Shek, *Appl. Phys. Lett.*, 2006, **89**, 231902.

(63) V. Demarne and A. Grisel, *Sens. Actuators*, 1988, **13**, 301.

(64) O. Dos Santos, M. L. Weiller, D. Q. Junior and A. N. Medina, *Sens. Actuators B*, 2001, **75**, 83.

(65) S. Shukla, S. Seal, L. Ludwing and C. Parish, *Sens. Actuators B*, 2004, **97**, 256.

(66) S. Harbeck, A. Szatvanyi, N. Barsan, U. Weimar and V. Hoffmann, *Thin Solid Films*, 2003, **436**, 76.

(67) H. Windischmann and P. Mark, *J. Electrochem. Soc.*, 1979, **126**, 627.

(68) V. Lantto and P. Romppainen, *Surf. Sci.*, 1987, **192**, 243.

(69) P. Romppainen and V. Lantto, *J. Appl. Phys.*, 1988, **63**, 5159.

(70) Z. W. Chen, D. Y. Pan, B. Zhao, G. J. Ding, Z. Jiao, M. H. Wu, C. H. Shek, L. C. M. Wu and J. K. L. Lai, *ACS Nano*, 2010, **4**, 1202.

(71) C. H. Shek, J. K. L. Lai and G. M. Lin, *J. Phys. Chem. Solids*, 1999, **60**, 189.

(72) Z. W. Chen, S. Y. Zhang, S. Tan, J. G. Hou and Y. H. Zhang, *Thin Solid Films*, 1998, **322**, 194.

(73) J. Feder, *Fractal*, Plenum Press, New York, 1988, p15.

(74) H. R. Fallah, M. Ghasemi and A. Hassanzadeh, *Phys. E*, 2007, **39**, 69.

(75) Y. J. Kim, Y. T. Kim, H. K. Yang, J. C. Park, J. I. Han, Y. E. Lee and H. J. Kim, *J. Vac. Sci. Tech. A*, 1997, **15**, 1103.

(76) S. Zhu, Y. F. Lu, M. H. Hong and X. Y. Chen, *J. Appl. Phys.*, 2001, **89**, 2400.

(77) D. Kim and H. Lee, *J. Appl. Phys.*, 2001, **89**, 5703.

(78) S. Zhu, Y. F. Lu and M. H. Hong, *Appl. Phys. Lett.*, 2001, **79**, 1396.

(79) L. Berthe, R. Fabbro, P. Peyre, L. Tollier and E. Bartnicki, *J. Appl. Phys.*, 1997, **82**, 2826.

(80) J. G. Hou and Z. Q. Wu, *Phys. Rev. B*, 1989, **40**, 1008.

(81) Z. W. Chen, S. Y. Zhang, S. Tan, J. G. Hou and Y. H. Zhang, *J. Vac. Sci. Technol. A*, 1998, **16**, 2292.

(82) R. B. Cooper, G. N. Advani and A. G. Jordan, *J. Electron. Mater.*, 1981, **10**, 455.

(83) A. Cicera, A. Dieguez, R. Diaz, A. Cornet and J. R. Morante, *Sens. Actuators B*, 1999, **58**, 360.

(84) D. H. Wang, R. Kou, D. Choi, Z. G. Yang, Z. Nie, J. Li, L. V. Saraf, D. H. Hu, J. G. Zhang, G. L. Graff, J. Liu, M. A. Pope and I. A. Aksay, *ACS Nano*, 2010, **4**, 1587.

(85) A. C. Balazs, T. Emrick and T. P. Russell, *Science*, 2006, **314**, 1107.

(86) H. Zeng, J. Li, J. P. Liu, Z. L. Wang and S. H. Sun, *Nature*, 2002, **420**, 395.

(87) T. Ramanathan, A. A. Abdala, S. Srankovich, D. A. Dikin and M. Herrera-Allonso, *Nature Nanotechnology*, 2008, **3**, 327.

(88) D. S. L. Abergel and V. I. Fal'ko, *Phys. Rev. B*, 2007, **75**, 155430.

(89) F. Wang, Y. B. Zhang, C. S. Tian, C. Girit, A. Zettl, M. Crommie and Y. R. Shen, *Science*, 2008,

320, 206.

(90) R. R. Nair, P. Blake, A. N. Grigorenko, K. S. Novoselov, T. J. Booth, T. Stauber, N. M. R. Peres and A. K. Geim, *Science*, 2008, **320**, 1308.

(91) M. S. Dresselhaus and G. Dresselhaus, *Adv. Phys.*, 2002, **51**, 1.

(92) M. Hirata, T. Gotou, S. Horiuchi, M. Fujiwara and M. Ohba, *Carbon*, 2004, **42**, 2929.

(93) M. F. Yu, O. Lourie, K. Moloni, T. F. Kelly and R. S. Ruoff, *Science*, 2000, **287**, 637.

(94) C. Berger, Z. M. Song, T. B. Li, X. B. Li, A. Y. Ogbazghi, R. Feng, Z. T. Dai, A. N. Marchenkov, E. H. Conrad, P. N. First and W. A. D. Heer, *J. Phys. Chem. B.*, 2004, **108**, 19912.

(95) Y. Zhang, J. P. Small, M. E. S. Amori and P. Kim, *Phys. Rev. Lett.*, 2005, **94**, 176803.

(96) Y. Zhang, Y. W. Tan, H. L. Stormer and P. Kim, *Nature*, 2005, **438**, 201.

(97) K. S. Novoselov, A. K. Geim, S. K. Morozov, D. Jiang, M. I. Katsnelson, I. V. Grigorieva, S. V. Dubonos and A. A. Firsov, *Nature*, 2005, **438**, 197.

(98) S. Stankovich, D. A. Dikin, G. H. B. Dommett, K. M. Kohlhaas, E. J. Zimney, E. A. Stach, R. D. Piner, S. T. Nguyen and R. S. Ruoff, *Nature*, 2006, **442**, 282.

(99) C. P. Peng, B. D. Chen, Y. Qin, S. H. Yang, C. Z. Li, Y. H. Zuo, S. Y. Liu and J. H. Yang, *ACS Nano*, 2012, **6**, 1074.

(100) J. X. Zhu, Y. K. Sharma, Z. Y. Zeng, X. J. Zhang, M. Srinivasan, S. Mhaisalkar, H. Zhang, H. H. Hng and Q. Y. Yan, *J. Phys. Chem. C*, 2011, **115**, 8400.

(101) H. Kim, D. H. Seo, S. W. Kim, J. Kim and K. Kang, *Carbon*, 2011, **49**, 326.

(102) B. J. Li, H. Q. Cao, J. Shao, G. Q. Li, M. Z. Qu and G. Yin, *Inorg. Chem.*, 2011, **50**, 1628.

(103) S. Q. Chen and Y. Wang, *J. Mater. Chem.*, 2010, **20**, 9735.

(104) Z. S. Wu, W. C. Ren, L. Wen, L. B. Gao, J. P. Zhao, Z. P. Chen, G. M. Zhou, F. Li and L. M. Cheng, *ACS Nano*, 2010, **4**, 3187.

(105) B. Wang, X. L. Wu, C. Y. Shu, Y. G. Guo and C. R. Wang, *J. Mater. Chem.*, 2010, **20**, 10661.

(106) C. Xu, X. Wang, L. C. Yang and Y. P. Wu, *J. Solid State Chem.*, 2009, **182**, 2486.

(107) H. L. Wang, L. F. Cui, Y. Yang, H. S. Casalongue, J. T. Robinson, Y. Y. Liang, Y. Cui and H. J. Dai, *J. Am. Chem. Soc.*, 2010, **132**, 13978.

(108) L. Li, Z. P. Guo, A. J. Du and H. K. Liu, *J. Mater. Chem.*, 2012, **22**, 3600.

(109) J. W. Lee, A. S. Hall, J. D. Kim and T. E. Mallouk, *Chem. Mater.*, 2012, **24**, 1158.

(110) X. J. Zhu, Y. J. Zhu, S. Murali, M. D. Stoller and R. S. Ruoff, *ACA Nano*, 2011, **5**, 3333.

(111) B. J. Li, H. Q. Cao, J. Shao, M. Z. Qu and H. H. Warner, *J. Mater. Chem.*, 2011, **21**, 5069.

(112) Y. Q. Zou and Y. Wang, *Nanoscale*, 2011, **3**, 2615.

(113) Y. C. Qiu, K. Y. Yan, S. H. Yang, L. M. Jin, H. Deng and W. S. Li, *ACS Nano*, 2010, **4**, 6515.

(114) S. J. Ding, J. S. Chen, D. Y. Luan, F. Y. C. Boey, S. Madhavi and X. W. Lou, *Chem. Commun.*, 2011, **47**, 5780.

(115) S. L. Zhang, Y. Z. Zhang, S. P. Huang, H. Liu, P. Wang and H. P. Tian, *J. Phys. Chem. C*, 2011, **114**, 19284.

(116) Z. W. Chen, Z. Jiao, M. H. Wu, C. H. Shek, C. M. L. Wu and J. K. L. Lai, *Prog. Mater. Sci.*, 2011, **56**, 901.

(117) C. Chen, L. J. Wang, Y. Y. Liu, Z. W. Chen, D. Y. Pan, Z. Li, Z. Jiao, P. F. Hu, C. H. Shek, C. M. L. Wu, J. K. L. Lai and M. H. Wu, *Langmuir*, 2013, **29**, 4111.

(118) K. S. Novoselov, A. K. Geim, S. V. Morozov, D. Jiang, Y. Zhang, S. V. Dubonos, I. V. Grigorieva and A. A. Firsov, *Science*, 2004, **306**, 666.

(119) H. P. Liu, D. H. Long, X. J. Liu, W. M. Qiao, L. Zhan and L. C. Ling, *Electrochim. Acta*, 2009, **542**, 5782.

(120) X. Y. Wang, X. F. Zhou, K. Yao, J. G. Zhang and Z. L. Liu, *Carbon*, 2011, **49**, 133.

(121) P. C. Lian, X. F. Zhu, H. F. Xiang, Z. Li, W. S. Yang and H. H. Wang, *Electrochim. Acta*, 2010, **56**, 834.

(122) L. S. Zhang, L. Y. Jiang, H. J. Yan, W. D. Wang, W. Wang, W. G. Song, Y. G. Guo and L. J. Wan, *J. Mater. Chem.*, 2010, **20**, 5462.

(123) Z. F. Du, X. M. Yin, M. Zhang, Q. Y. Hao, Y. G. Wang and T. H. Wang, *Mater. Lett.*, 2010, **64**, 2076.

(124) A. Zhong, J. Z. Wang, Z. X. Chen and H. K. Liu, *J. Phys. Chem. C*, 2011, **115**, 25115.

(125) Y. X. Xu, H. Bai, G. W. Lu, C. Li and G. Q. Shi, *J. Am. Chem. Soc.*, 2008, **130**, 5856.

(126) J. F. Liang, W. Wei, D. Zhong, Q. L. Yang, L. D. Li and L. Guo, *ACS Appl. Mater. Interfaces*, 2012, **4**, 454.

(127) H. He, J. Klinowski, M. Forster and A. Lerf, *Chem. Phys. Lett.*, 1998, **287**, 53.

(128) A. Lerf, H. He, M. Forster and J. Klinowski, *J. Phys. Chem. B*, 1998, **102**, 4477.

(129) M. Hirata, T. Gotou and M. Ohba, *Carbon*, 2005, **43**, 503.

(130) T. Szabo, A. Szeri and I. Dekany, *Carbon*, 2005, **43**, 87.

(131) L. S. Zhong, J. S. Hu, Z. M. Cui, L. J. Wan and W. G. Song, *Chem. Mater.*, 2007, **19**, 4557.

(132) F. Tuinstra and J. L. Koenig, *J. Chem. Phys.*, 1970, **53**, 1126.

(133) S. M. Paek, E. J. Yoo and I. Honma, *Nano Lett.*, 2009, **9**, 72.

(134) C. E. Salmas and G. P. Androutsopoulos, *Langmuir*, 2005, **21**, 11146.

(135) D. Y. Zhao, J. L. Feng, Q. S. Huo, N. Melosh, G. H. Fredrickson, B. F. Chmelka and G. D. Stucky, *Science*, 1998, **279**, 548.

(136) L. Noerochim, J. Z. Wang, S. L. Chou, H. J. Li and H. K. Liu, *Electrochim. Acta*, 2010, **56**, 314.

(137) Y. Wang, H. C. Zeng and J. Y. Lee, *Adv. Mater.*, 2006, **18**, 645.

(138) P. C. Lian, X. F. Zhu, S. Z. Liang, Z. Li, W. S. Yang and H. H. Wang, *Electrochim. Acta*, 2011, **56**, 4532.